

**DESIGN AND ANALYSIS OF PLASMONIC  
NANOANTENNAS WITH GROUND PLANE  
AND IMPEDANCE MATCHING**

by

**Adeel Afridi**

A Dissertation Submitted to the  
Graduate School of Sciences and Engineering  
in Partial Fulfillment of the Requirements for  
the Degree of  
Master of Science

in

Electrical and Electronics Engineering



**KOÇ  
UNIVERSITY**

August 16, 2016

**DESIGN AND ANALYSIS OF PLASMONIC NANOANTENNAS  
WITH GROUND PLANE AND IMPEDANCE MATCHING**

Koç University

Graduate School of Sciences and Engineering

This is to certify that I have examined this copy of a master's thesis by

**Adeel Afridi**

and have found that it is complete and satisfactory in all respects,  
and that any and all revisions required by the final  
examining committee have been made.

Committee Members:

---

Asst. Prof. Şükrü Ekin Kocabaş (Advisor)

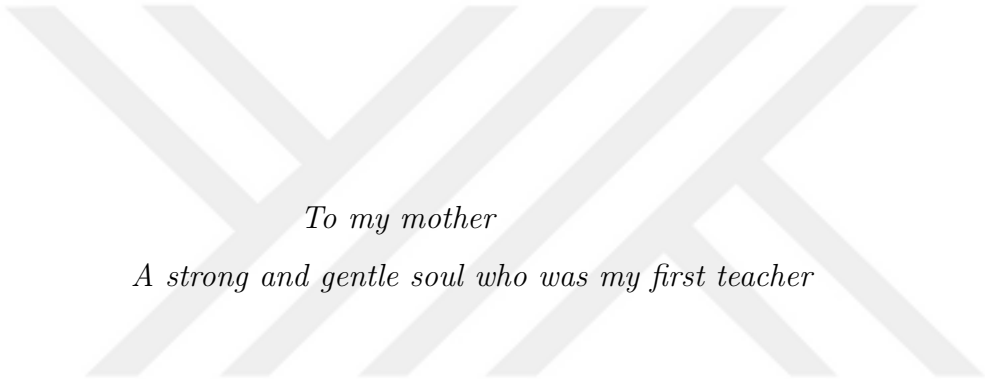
---

Prof. İsmail Karakurt

---

Asst. Prof. Sedat Nizamoğlu

Date: \_\_\_\_\_



*To my mother*  
*A strong and gentle soul who was my first teacher*

*To my siblings and nephew*

*To the memory of my father*  
*Who was often in my thoughts on this journey - you are missed*

## ABSTRACT

There is wide spread ongoing research in the field of plasmonics due to its diverse applications in many fields such as wireless nano-links, laser detection and ranging (LADAR), nano-scale waveguides, high efficiency solar cell, nano-scale lasers, invisibility cloaking, and cancer treatment, to name a few. Plasmonic devices have the ability to concentrate, guide and manipulate light below diffraction limit, thus offering advantages like optical bandwidth and densely integrated circuitry within few microns. However, among many challenges, major concern is to efficiently couple and localize light at such scale. Recently, metallic optical nanoantennas are widely used for efficient coupling and concentrating of light. Nanoantennas' ability to support surface plasmons, and their inherited traits from conventional radio frequency (RF) antennas, makes them excellent candidates for plasmonic applications.

This thesis investigates widely used RF antenna, known as horn antenna, in optical frequencies. Structure of horn nanoantenna consists of Two Wire Transmission Line (TWTL) flared in one axis. Plasmonic horn nanoantenna offer advantages like ease of fabrication, inherent matched coupling with TWTL, high end-fire directivity, and high efficiency. We start our analysis by investigating the effect on radiation behavior of the nanoantenna, when placed on the interface of two different semi-infinite substrates. In this case, we demonstrate that the nanoantenna radiates significant power into material with high permittivity, thus no longer radiating end-fire. In order to control radiation direction of the horn nanoantenna, we employ metallic ground plane at the back of substrate with high permittivity, and achieve beam steering, in wide range of radiation angles, by varying metal-backed substrate's thickness. We observe that metal-backed substrate increase the back reflection of power from the flares into TWTL. To minimize the back reflection, we employ impedance matching technique,

which improves matching by more than 70%, and more than 99.75% of power is delivered to the nanoantenna. In addition, we propose analytical model for impedance matching technique which accurately predict optimal parameters to achieve minimum back reflection.



## ÖZETÇE

Kablosuz nano bağlantı, lazer ile mesafe tespiti (LADAR), nano boyutlu dalga kılavuzları, nano boyutlu lazerler, yüksek verimlilikli güneş gözeleri, görünmezlik pelerini ve kanser tedavisi gibi çeşitli uygulamalar nedeniyle plazmonik alanında araştırmalar yaygındır. Plazmonik aygıtların ışığı kırınım limitinin altına odaklama ve yönlendirme becerisi sayesinde optik bant aralığını ve yoğun entegre devreleri birkaç mikrona sığdırmak artık mümkündür. Ancak ışığı bu boyutlara odaklamak ve bu boyutlardaki aygıtlarla eşleştirmek büyük bir zorluk teşkil etmektedir. Yakın zamanda metalik optik nano antenler ışığın eşleştirilmesi ve odaklanması için kullanılmıştır. Nano antenlerin yüzey plazmonlarını destekleme özelliği ve geleneksel radyo frekansı (RF) antenlerden miras aldığı özellikler, onları plazmonik uygulamalar için mükemmel adaylar pozisyonuna getirmektedir.

Bu tezde sıkça kullanılan ve boynuz anten olarak bilinen radyo frekansı anteninin optik frekanslarda incelenmesi amaçlanmıştır. Boynuz nano anteninin bir iki telli iletim hattının (TWTL) tek eksende genişletilmiş bir yapıya sahiptir. Plazmonik boynuz nano anten kolay üretim, iki telli iletim hattının (TWTL) ile doğal eşleşme, yüksek uçtan ışımaya yönlülüğü ve yüksek verimlilik gibi avantajlara sahiptir. Analizimize nano anteninin iki farklı yarı-sonsuz ortamı ayıran arayüzdeki ışımaya davranışını inceleyerek başladık. Bu durumda nano antenlerin yüksek dielektrik geçirgenliğe sahip materyalin içine ışımaya yaptığını gözlemledik, dolayısıyla artık uçtan ışımaya yapmıyorlardı. Boynuz nano antenlerin ışımaya yönünü kontrol etmek için yüksek geçirgenliğe sahip alt katmanın arkasına metalik bir plaka yerleştirdik. Bu şekilde arka yüzünde metal plaka olan alt katmanın genişliğini değiştirerek ışın demetini büyük bir açı aralığında yönlendirebildik. Metal plakanın optik gücün genişletilmiş bölümden iki telli iletim hattının düz kısmına geri yansımaya arttırdığını gözlemledik. Bu geri yansımaya en aza in-

dirmek için, empedans eşleştirme tekniğine başvurduk. Bu teknik eşleştirmeyi % 70 arttırdı ve giriş gücünün % 99.75'i nano antene iletildi. Ek olarak empedans eşleştirme tekniği için en az geri yansımayı sağlayan uygun parametreleri bulan bir analitik model önerdik.



## ACKNOWLEDGMENTS

First and foremost, I would like to express my sincere gratitude and deepest appreciation to my supervisor Asst. Prof. Şükrü Ekin Kocabaş for his never ending support, guidance, and efforts. Without his help, advice, expertise, patience and encouragement, this research and thesis would have been almost impossible. He not only played a role of advisor, but also a leader, friend and hero. I would also like to thank the other members of my thesis committee: Asst. Prof. Sedat Nizamoğlu, and Prof. Ismail Karakurt. Their insight, feedback, and advice was influential and essential throughout writing process. I feel lucky on having such humble people on my thesis committee.

I am also grateful to all those teachers with whom I took courses throughout my M.Sc. studies, specifically, I would like to thank Prof. Irşadi Aksun, and Prof. Ali Serpengüzel for their everlasting support and guidance.

I would specially thank to the group members of Nanophotonics Research Group: Solmaz Nagihzadeh, Ongun Arısev, and Aziz Karaşahin. From Solmaz and Aziz, I learned simulation and experimental skills. They helped me in all aspects whenever I got stuck in my research. I wish both success for their PhD studies, and would be eagerly waiting to address them by the title of Doctor.

I feel obliged to express my deepest appreciation to my dear friends Ongun Arısev and Sasan Asadi Abadi. We started the journey of M.Sc. together, and at each step they were there for me as best friends, brothers, and partners in crime. We have laughed together and they were also been kind when I needed to cry. When others doubted, they remained a fan. When I became too serious, their humor and friendly sarcasm allowed me to laugh and lightened my perspective. They did not only helped me in my academics, but also in every day life. I am eternally in-debt to them for

their kindness, friendship, gym training, and coding and English language skills.

Peaceful environment is essential and necessary for peace of mind and graduate studies. I would like to thank Muhammad Nufail Farooqi for providing peaceful environment at apartment. Nufail is not only among best friends, but also an elder brother. He is the only reason that our student apartment feels so lively, and a home. He is the person I could rely on.

Three other friends I must mention are Rizwan Sadiq, Altynbek Isabekov, and Hazan Ezgi Imer. All of them were bothering officemates but best humans and friends, I could ever have. I found Rizwan's home as my second home here in Istanbul, where I was and hopefully always be invited open heartedly. I would like to thank Hazan for her world best börek, Turkish language lessons, and translations. I would also thank Altynbek for polishing my  $\text{\LaTeX}$  and MATLAB skills, and consider him as guru of coding.

I would also take this opportunity to thank Pakistani community here at Koç university. They always made me feel like home. Especially, I would like to thank Aatif Ijaz, Abdul Rehman, Muhammad Zakwan, Naveed Ahmed Abbasi, Nabil Khalid, Shoaib Soomro, Suhaib Afridi, Ali Mughal, Haris Shehzad Marwat, and Talha Irfan. I will always miss their gatherings.

I would like to also acknowledge my childhood best friends: Muhammad Umer, Omaid Wazir, Hashmat Ullah, Asim Haider, and Zahoor Ahmed. All of them played important part in making me what I am today.

Last but not the least, my special thanks go to my family, particularly to my lovely mother, a strong and gentle soul who taught me to trust in myself, believe in hard work, and helped me overcome the challenge of studying abroad. I am also deeply thankful to my father for earning an honest living for us and for supporting us till last of his breath. I am also lucky to have friend like siblings: Aftab Khan, Ambreen Khan, Adnan Afridi, and Kiran Afridi. I am thankful to Aftab Khan and Ambreen Khan for their efforts in raising us after my father, Adnan Khan for being best friend

at home, and Kiran Afridi whom I am proud of for being such an intelligent child. I also dedicate this thesis to my lovely nephew Ammar Aftab who is the pride and joy of my life.

I would like to thank TÜBİTAK (The Scientific and Technical Research Council of Turkey) and Koç University for providing me scholarship which made my study, a step to my goal, and dreams possible.



# TABLE OF CONTENTS

<b>List of Figures</b>	<b>xiv</b>
<b>Chapter 1: Introduction</b>	<b>1</b>
1.1 Thesis outline . . . . .	2
<b>Chapter 2: Background theory</b>	<b>4</b>
2.1 Literature review . . . . .	4
2.2 Metals at optical frequencies . . . . .	6
2.3 Surface plasmon . . . . .	7
2.4 TWTLs . . . . .	12
2.5 Basic definitions of Antenna theory . . . . .	16
2.5.1 Radiation pattern . . . . .	16
2.5.2 Directivity . . . . .	16
2.5.3 Principal patterns, E-plane and H-plane . . . . .	17
2.5.4 Reflection coefficient . . . . .	17
<b>Chapter 3: Plasmonic Horn Nanoantenna</b>	<b>18</b>
3.1 Antenna structure . . . . .	18
3.2 Simulation setup . . . . .	18
3.2.1 Selection of Physics and Study Steps . . . . .	19
3.2.2 Geometry . . . . .	19
3.2.3 Boundary Conditions . . . . .	20
3.2.4 Materials . . . . .	20
3.2.5 Excitation Port . . . . .	21

3.2.6	Mesh . . . . .	22
3.2.7	Far-field Calculation . . . . .	23
3.3	Antenna in homogeneous medium . . . . .	23
3.4	Antenna on interface between heterogeneous media (Air and Glass) . . . . .	24
3.5	Antenna on metal-backed ground plane - beam steering . . . . .	28
<b>Chapter 4: Impedance Matching</b>		<b>35</b>
4.1	Impedance matching . . . . .	36
4.2	Analytical model for impedance matching . . . . .	36
4.3	Simulation vs. analytical model . . . . .	40
<b>Chapter 5: Fabrications, Optical Setup, and Measurements</b>		<b>44</b>
5.0.1	Change of geometrical parameters of the horn nanoantenna . . . . .	44
5.1	Fabrication . . . . .	44
5.1.1	Dicing . . . . .	45
5.1.2	Cleaning . . . . .	45
5.1.3	Spin coating with PMMA . . . . .	45
5.1.4	Aluminum metalization . . . . .	46
5.1.5	E-beam lithography . . . . .	46
5.1.6	Aluminum removal . . . . .	46
5.1.7	PMMA development . . . . .	47
5.1.8	Titanium and gold coating . . . . .	47
5.1.9	Lift-off . . . . .	47
5.1.10	SU-8 coating . . . . .	48
5.2	Optical setup . . . . .	50
5.3	Measurements . . . . .	52
5.3.1	Measurement methodology . . . . .	52
5.3.2	Measurements . . . . .	55

**Chapter 6: Conclusion**

**59**

**Bibliography**

**61**



## LIST OF FIGURES

2.1	Relative permittivity of Gold (Au) based on Drude and Lorentz-Drude model. . . . .	8
2.2	Metal-dielectric waveguide. . . . .	9
2.3	Dispersion relation of SPP at MD interface, with gold and quartz . .	11
2.4	Geometry of three layered system (MDM or DMD) where layer 1 (metal or dielectric) is sandwiched between two semi-infinite media (dielectric or metal) . . . . .	12
2.5	Mode profile of a) odd parity SPPs and b) even parity SPPs for MDM structure [Dionne et al., 2006] . . . . .	13
2.6	Mode profile of TWTL in homogeneous media (quartz) at $1.55 \mu\text{m}$ wavelength. . . . .	14
2.7	Propagation constant $\beta$ , and Propagation Length $L_p$ for TWTL in homogeneous and heterogeneous media . . . . .	15
2.8	Radiation pattern (power pattern) in coordinate system [Balanis, 2016].	16
3.1	Schematics of plasmonic sectoral horn antenna. . . . .	18
3.2	Basic 2-D Structure of plasmonic horn nanoantenna using Polygon feature. . . . .	20
3.3	3-D finalized structure of plasmonic horn nanoantenna after using “Extrude” and “Convert to Solid” features. . . . .	20
3.4	Plasmonic horn nanoantenna inside a PML cubic box. . . . .	21
3.5	Excitation port for plasmonic horn nanoantenna. . . . .	21
3.6	Meshing of geometry in COMSOL. . . . .	22
3.7	Plasmonic horn antenna enclosed in glass. . . . .	23

3.8	Plasmonic horn antenna near-field $E_y$ intensity plots for $t = 100\text{nm}$ , $\theta = 26.6^\circ$ , and different specified $l$ . . . . .	25
3.9	Plasmonic horn antenna directivity for $t = 100\text{nm}$ , $\theta = 26.6^\circ$ , and different specified $l$ . . . . .	26
3.10	Amplitude reflection coefficient ( $S_{11}$ ) of plasmonic horn nanoantenna with $l = 1000\text{nm}$ . . . . .	27
3.11	Plasmonic horn nanoantenna on glass substrate with $l = 650\text{nm}$ , $t = 300\text{nm}$ , and $\theta = 20^\circ$ . . . . .	28
3.12	Results for plasmonic horn nanoantenna placed over infinite glass substrate. (a) top view of 2-D $E_y$ field in XY-plane. (b) side view of 2-D $E_y$ field in XZ-plane. (c) H-plane directivity pattern. (d) Amplitude reflection coefficient $\Gamma$ in linear scale (black solid-line). . . . .	29
3.13	Total radiation efficiency (orange + -line), radiation efficiency in substrate (red broken-line), and radiation efficiency in air (blue line). . .	30
3.14	Plasmonic horn nanoantenna on metal-backed substrate with substrate thickness $d$ . . . . .	31
3.15	(a) Side view of near-field $E_y$ intensity for $d = 300\text{nm}$ . (b) Side view of near-field $E_y$ intensity for $d = 500\text{nm}$ . (c) H-plane directivity pattern for $d = 300\text{nm}$ . (d) H-plane directivity pattern for $d = 500\text{nm}$ . . . . .	32
3.16	Elevation angle $\theta$ (angle of maximum directivity) as function of thickness $d$ of substrate. . . . .	33
3.17	Amplitude reflection coefficient of the nanoantenna backed by plasmonic substrate for $d = 300\text{nm}$ . . . . .	34
4.1	Plasmonic horn nanoantenna with impedance matching section (IM) with length $l_2$ and slot filled with glass (Ag-glass-Ag). . . . .	37

4.2	Analytical model for impedance matching. (a) Ag-air-Ag TWTL with plasmonic horn. (b) Ag-air-Ag TWTL cascaded with Ag-dielectric-Ag TWTL. . . . .	38
4.3	Reflection coefficient calculated from analytical model as function of $l_1$ and $l_2$ . . . . .	39
4.4	Comparison of reflection coefficient of ground-plane backed plasmonic horn antenna with $l_1 = 350\text{nm}$ and $l_2 = 125\text{nm}$ , $l = 650\text{nm}$ , $t = 300\text{nm}$ , $\theta = 20^\circ$ , and $d = 300\text{nm}$ . Case 1 refers to result from analytical model, Case 2 refers to result from simulation, while Case 3 is result for antenna without impedance matching. . . . .	41
4.5	Comparison of reflection coefficient of ground-plane backed plasmonic horn antenna with $l_1 = 50\text{ nm}$ and $l_2 = 100\text{ nm}$ , $l = 650\text{ nm}$ , $t = 300\text{ nm}$ , $\theta = 20^\circ$ , and $d = 300\text{ nm}$ . Blue line shows result from analytical model, while red line shows result from simulation. . . . .	42
4.6	H-field directivity pattern for metal-backed plasmonic horn nanoantenna with impedance matching section. . . . .	43
5.1	SEM image of plasmonic horn nanoantenna integrated with bend waveguide. . . . .	48
5.2	SEM image of plasmonic horn nanoantenna integrated with mode converter. . . . .	48
5.3	Fabrication process of plasmonic horn nanoantenna, in summary. . . . .	49
5.4	Schematics of optical setup based on reflective microscopy. . . . .	51
5.5	Image of plasmonic horn nanoantenna coupled to bend waveguide, taken with our optical setup. . . . .	52
5.6	Image of beam incident on sample when P1 and P2 are in parallel. . . . .	53
5.7	Image of beam incident on sample when P1 and P2 are in cross. . . . .	53

5.8	Image of plasmonic nanoantenna coupled with bend slot waveguide, with beam shinning on input nanoantenna . . . . .	54
5.9	Image of plasmonic nanoantenna coupled with bend slot waveguide, with beam shinning on input nanoantenna, and without illumination. . . . .	54
5.10	Propagation length ( $L_0$ ) of slot waveguide with $g = 220$ nm. . . . .	56
5.11	$T_{total}(\lambda)$ of six devices with same geometrical parameters with in same optimal dose. . . . .	57
5.12	Comparison of transmission $T_{ant}$ of plasmonic horn nanoantenna for measured results (A1 to 6). . . . .	58



## Chapter 1

### INTRODUCTION

Semiconductor devices are famous for their performance, speed, and feasibility to use. These characteristics of semiconductor devices depend on their miniaturization and integration with other devices. However, operational characteristics like bandwidth and speed of these electronic semiconductor already reached to its limitation, which is serious concern for advancement of scientific and technological field [Gramotnev and Bozhevolnyi, 2010]. One possible solution is to modulate information on light signal, instead of electronic signal, as light communication provides much superior speed than their electronic counterpart. However, performance of photonic devices is also limited by diffraction limit [Born and Wolf, 2000]. Diffraction limit does not allow localization of light wave or electromagnetic wave in nanoscale region much smaller than wavelength.

Another solution is to make use of negative permittivity material to localize light wave in sub-wavelength devices as small as few nanometers. Metals have negative permittivity above plasma frequency. Metal and dielectric interfaces above plasma frequency can localize light under certain suitable conditions in the form of surface plasmon-polaritons (SPPs) [Raether, 1988]. SPPs are electromagnetic wave or light wave coupled to collective oscillation of electron density on metal-dielectric interface. These are hybrid nature of wave with characteristics of both light wave and electrons. First pioneered by Rufus Ritchie [Dionne and Atwater, 2012], the history of SPPs track back to millennia where glass makers and chemists took advantage of it unknowingly [Atwater, 2007]. In 2000, Atwater group at California Institute of Technology first tossed the name “Plasmonics” to this study of SPPs at metal-dielectric

Interface [Atwater, 2007]. This so called “Plasmonics” opened gates for new area of research where field of photonics and electronics merges at nanoscale. These surface plasmons (SPs) or SPPs can serve as basis of devising nanoscale photonic circuit. In addition, SPPs can serve as basis for devising sub-wavelength waveguides and nanoantennas, which in turn serves as basic component of any circuitry for signal carriage and localization.

Optical antennas or nano-antennas have been focus of research efforts for this past decade due to their intriguing applications in wireless nano-link [Yang et al., 2016, Yang et al., 2014, Huang et al., 2009, Alù and Engheta, 2010, Solís et al., 2013], nanoscale spectroscopy [Bharadwaj et al., 2011], photo voltaic devices [Atwater and Polman, 2010], photo-detection [Knight et al., 2011], photo emission [Curto et al., 2010, G. et al., 2011], biosensing [Anker et al., 2008], and nonlinear plasmonics [Kauranen and Zayats, 2012]. However, adaptation of conventional antenna theory and design technique is not straight forward in the optical frequencies, due to the fact that metal’s behavior is different at these frequencies. In optical frequency regime, metals cannot be regarded as perfect conductors, and support surface plasmon polaritons (SPP) [Novotny, 2007, Ramaccia et al., 2011]. Downscaling of antenna design to optical frequencies is not the only concern of researchers of the field. Fabrication of nanoantenna structures, impedance matched integration with waveguides or Two Wire Transmission Line (TWTL), and efficient energy extraction from (or coupling to) these antennas or directivity control are challenges that are also faced by researchers [Huang et al., 2009, Ramaccia et al., 2011, Xu et al., 2011, Sachkou et al., 2011, Ginzburg and Orenstein, 2007].

### **1.1 Thesis outline**

In Chapter 2, we discuss background information required for the concept of plasmonic nanoantennas and give a brief literature review. We start our discussion with introduction to surface plasmon, and behavior of metals at optical frequencies. We give insight of plasmonic slot waveguide and Two Wire Transmission Line (TWTL). We discuss modes supported by waveguides and TWTLs. Afterwards, we give some

basic definition related to antenna theory, which are used in the scope of this thesis.

In Chapter 3, We present full analysis of plasmonic horn nanoantenna. We discuss step-by-step simulation strategy in FEM based solver, COMSOL MULTIPHYSICS, adopted for analyzing the nanoantenna. We investigate horn nanoantenna inside homogeneous medium, on the interface of two different medium, and on metal-backed substrate. We demonstrate the effect of each of these case on the nanoantenna operation.

In Chapter 4, we discuss about the impedance matching technique used to matched the nanoantenna with TWTL. In addition, we present analytical model for modeling the back reflection of horn into TWTL. We demonstrate that our model accurately predicts optimal geometrical parameters of impedance matching section for high matching. In addition, we validate our model with simulated results.

Chapter 5 is about the fabrication, and optical characterization of horn nanoantenna. We present a detailed, step-by-step, process used to fabricate plasmonic horn nanoantenna. We give a full insight of our optical setup, which was used to characterize plasmonic nanoantennas. Finally, we discuss methodology of measurements employed for characterization, and present with measured results for plasmonic horn nanoantenna.

## Chapter 2

### BACKGROUND THEORY

#### 2.1 *Literature review*

Antennas play a vital role, as a mediator between free space propagation and localized energy [Yang et al., 2016], in any communication system. Specifically in the case of optical wireless nano-links, apart from their role as a mediator, antennas may offer less loss and improved performance, for propagation distance of few wavelength, as compared to their plasmonic waveguide interconnect counterparts [Yang et al., 2016, Alù and Engheta, 2010].

For downscaling antenna design rule to optical frequencies, [Novotny, 2007] proposed effective wavelength scaling of antennas. In conventional antenna design, length of antenna is related to wavelength of impinging wave, but in optical frequency regime length is a function of material dependent shorter effective wavelength.

Recently, a widespread used antenna in RF counterpart known as horn antenna [Balanis, 2016] has been extended to optical frequency regime which offer advantages such as: an inherently integrated and matched TWTL with radiating element, ease of power extraction, high directivity, and efficiency [Yang et al., 2016, Yang et al., 2014, Ramaccia et al., 2011]. Ramaccia et al. first studied horn nanoantenna with gradual exponential tapered structure [Ramaccia et al., 2011]. Metal-Insulator-Metal waveguide with cylindrical metallic pillars was incorporated as TWTL for that nanoantenna. Proposed antenna showed wide band and efficient response. Similar structure was adopted by Yang et al. [Yang et al., 2014] where they designed a broadband and highly directive E-plane horn [Balanis, 2016] nanoantenna with straight flares fully incorporated in homogeneous medium. In [Yang et al., 2016], Yang et al. extended the same horn antenna concept with modified structure, where horn was carved into the

metal along a channel waveguide. Both, [Yang et al., 2016] and [Yang et al., 2014], presented a systematic study of horn antenna for different flare parameters, and in addition wireless nano-link was implemented as application of horn antenna.

Nanoantennas presented in [Yang et al., 2016, Yang et al., 2014, Ramaccia et al., 2011] have high directivity, and are suitable for wireless nano-links, or other such applications, where nanoantenna are required to radiate end-fire. Thus, there is need to engineer radiation of these end-fire, highly directive antennas such that they radiate broadside [Balanis, 2016], or in any given direction, for other applications like laser detection. In addition, these aforementioned end-fire antennas were analyzed and designed in homogeneous medium. On other hand, antenna placed on interface of two different media, with substrate of higher permittivity than cladding layer, radiates significant power into substrate; thus, a fraction of power can be coupled or extracted [Curto et al., 2010, G. et al., 2011], as antenna will not radiate end-fire. Previously, plasmonic substrates, or metallic ground-planes were used to manipulate the nanoantennas' radiation [Xi et al., 2013, Min et al., 2011, Ahmed and Gordon, 2011, Seok et al., 2011, Ghadarghadr et al., 2009]. If a reflector ground plane is employed, direct emitted light from the nanoantenna and reflected light from ground plane, acting as image antenna, can interfere with different phases, enabling one to control and engineer the far-field radiation [Ghadarghadr et al., 2009, Xi et al., 2013]. In [Ghadarghadr et al., 2009], Shabnam Ghadarghadr et al. reported that dipole nanoantenna far-field radiation can be engineered, by changing distance between the dipole and reflecting surface, and showed beam steering can be achieved in any arbitrary direction, ranging from end-fire to broadside. Similarly, reflector ground planes were also used by [Min et al., 2011, Ahmed and Gordon, 2011, Seok et al., 2011] in order to direct the scattered radiation from nanoparticles or dipole nanoantenna out of the substrate plane, for application of Raman spectroscopy.

## 2.2 Metals at optical frequencies

At microwave frequencies, metals are considered as Perfect Electric Conductor (PEC) because, at these frequencies, metals significantly attenuates the electromagnetic waves when impinged on them. However, this is not the case for infrared and optical frequencies, where the metal behaves as lossy dielectrics with high real part of complex permittivity, unlike in the case of microwaves where metals have significantly large imaginary part of permittivity. At infrared and optical frequencies, metals support surface plasmon polaritons (SPPs) — a hybrid nature of wave that are light waves (photons) coupled to density waves of electrons on the metal surface.

Metals have free electron and bounded electrons in its valance shell. Upon infrared and optical frequencies, free electrons moves with impinging photons, and leads to intra-band absorption in metals. On other hand, bounded electrons leads to inter-band absorption, and oscillates harmonically when such waves imping on metals [Bohren and Huffman, 2008]. In short, both free electrons and bounded electrons contribute to the large negative real part of complex permittivity. Since in this thesis, we are using noble metal, gold, for nanoantennas, therefore it is very important to understand the dispersive nature metals as a function of frequencies. In literature, both analytical models [Economou, 1969, Burke et al., 1986], and experimental data has been used to model the dispersive permittivity of metals, in order to study plasmonic structures [Yang et al., 2014, Yang et al., 2016]. The common theoretical models which are used for metals' behavior are Drude, Lorentz, Drude - Lorentz, and Drude - Debye.

Drude model is the simplest of model, which captures the effect of free-electron motion, and intra-band absorption on the dispersive behavior of the metals. Relative permittivity  $\varepsilon_r(\omega)$  according to Drude model is given as follows

$$\varepsilon_r(\omega) = 1 - \frac{\omega_p^2}{\omega^2 - j\gamma\omega} \quad (2.1)$$

Where  $\omega_p$  is plasma frequency, and  $\gamma$  is the average collision frequency. Although, Drude model is simple and adequate model, but it does not take the effect of bounded

electrons into account, which significantly effects the permittivity at some specific frequencies [Bohren and Huffman, 2008]. On other hand, Lorentz model, a harmonic oscillator model, captures the effect of bounded electrons, but not free electrons, and model is given by equation as follow

$$\varepsilon_r(\omega) = 1 + \frac{\omega_p^2}{\omega_o^2 - \omega^2 + j\gamma\omega} \quad (2.2)$$

Where  $\omega_o^2$  is the resonance frequency of Lorentz harmonic oscillator. Thus in order to capture the total effect of SPPs, at infrared and optical frequencies, Lorentz - Drude model is considered and accurate model which captures both intra-band and inter-band effects. Model is shown as

$$\varepsilon_r(\omega) = \varepsilon_r(\omega)^{free} + \varepsilon_r(\omega)^{bound} \quad (2.3)$$

$$\varepsilon_r(\omega) = 1 - \frac{\omega_{pf}^2}{\omega^2 - j\gamma_e\omega} + \sum_n \frac{\omega_{pn}^2}{\omega_{0n}^2 - \omega^2 + j\gamma_n\omega} \quad (2.4)$$

Where  $e$  in the subscript refers to free electron, while  $n$  represents  $n^{th}$  Lorentz oscillator for bounded electron model. Figure 2.1 shows relative permittivity calculated based on Drude and Lorentz-drude model.

Throughout in this research, we used experimental data sets for complex relative permittivity of noble metals like gold and silver. The experimental data set is obtained from Palik's [Palik, 1998]. Another popular data set is by Johnson and Christy [Johnson and Christy, 1972a]

### 2.3 Surface plasmon

In this section we give a brief introduction about surface plasmons (SPs) on 2-D metal-dielectric (MD), and three layered metal-dielectric-metal (MDM) or dielectric-metal-dielectric (DMD) interfaces. In order to give background about TWTL, it is necessary to discuss these basic structures. In depth analysis, and derivation can be found in [Economou, 1969, Dionne et al., 2006]. The simplest geometry for localization of SPs is single layered metal-dielectric (MD) interface as shown in Figure 2.2 where dielectric is semi-infinite half space ( $x > 0$ ) with positive real dielectric constant  $\varepsilon_2$  and other

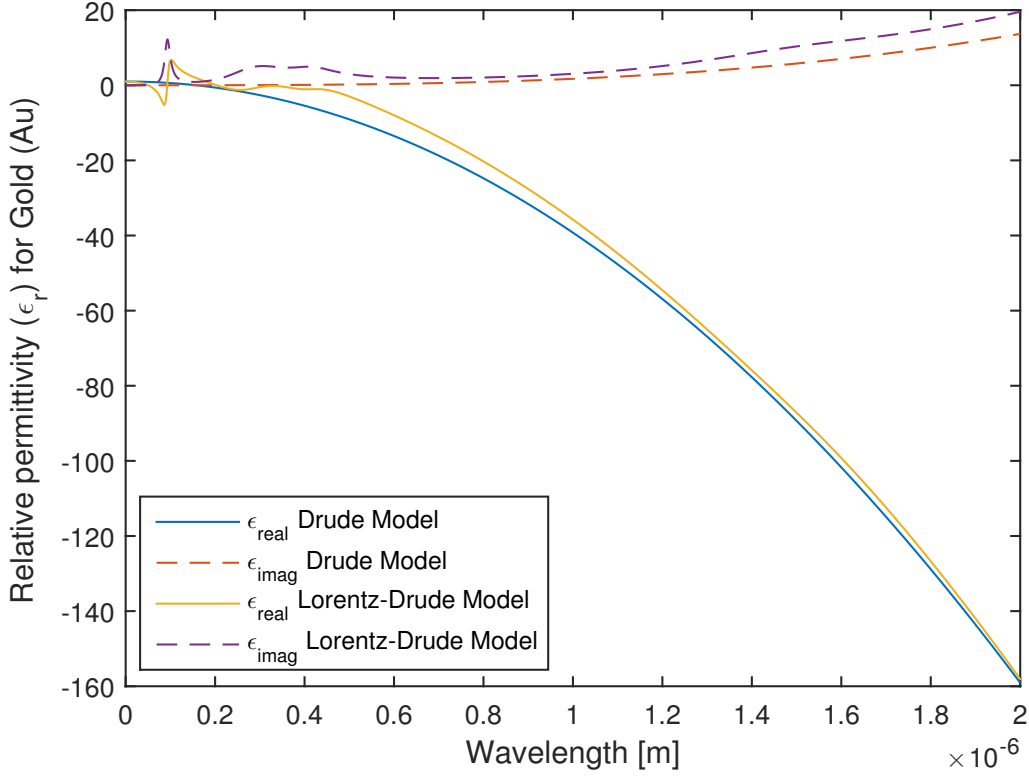


Figure 2.1: Relative permittivity of Gold (Au) based on Drude and Lorentz-Drude model.

half space ( $x < 0$ ) as absorbing metal with dielectric constant as function of frequency  $\epsilon(\omega)_1$ . Since for surface plasmon to be confined the requirement for dielectric constant of metal is to be negative real value thus implying  $\text{Re}\{\epsilon(\omega)_1\} < 0$ . Now the aim is to look for propagating wave solutions in x-direction confined to interface.

In order to investigate the physical properties such as dispersion relation of MD interface, one can apply conventional Maxwell's equation to come up with wave equation as follow.

$$\nabla^2 E - \frac{\epsilon \partial^2 E}{c^2 \partial t^2} = 0 \quad (2.5)$$

Now let us consider harmonic dependence of Electric field  $E(r, t) = E(r)e^{-i\omega t}$ . Insert



Figure 2.2: Metal-dielectric waveguide.

this in equation 2.5 to get Helmholtz equation of form

$$\nabla^2 E + k_0^2 \varepsilon E = 0 \quad (2.6)$$

Where  $k_0 = \omega/c$  is the wave vector propagating in free space. Since defined geometry is one-dimensional simple geometry where wave propagates in x-direction and there is no spatial variation in y-direction thus the propagating field can be defined as  $E(x, y, z) = E(z)e^{i\beta x}$  where the complex parameter  $\beta$  is called propagation constant of propagating wave in x-direction. Inserting definition of E-field in equation 2.7 yields

$$\nabla^2 E + (k_0^2 \varepsilon - \beta^2) E = 0 \quad (2.7)$$

And similar equation exists for H-field. Now equation 2.7 has to be solve separately in each region of constant  $\varepsilon$  and the solutions can be obtained by applying appropriate boundary conditions. There can be two possible solutions i.e. 1) TE and 2) TM solution. Let us first observe TM solutions.

$$H_y(z) = A_2 e^{i\beta x} e^{-k_2 z} \quad (2.8)$$

$$E_x(z) = iA_2 \frac{1}{\omega \varepsilon_0 \varepsilon_2} k_2 e^{i\beta x} e^{-k_2 z} \quad (2.9)$$

$$E_z(z) = -A_2 \frac{\beta}{\omega \varepsilon_0 \varepsilon_2} e^{i\beta x} e^{-k_2 z} \quad (2.10)$$

For  $z > 0$

$$H_y(z) = A_1 e^{i\beta x} e^{-k_1 z} \quad (2.11)$$

$$E_x(z) = iA_1 \frac{1}{\omega \varepsilon_0 \varepsilon_2} k_1 e^{i\beta x} e^{-k_1 z} \quad (2.12)$$

$$E_z(z) = -A_1 \frac{\beta}{\omega \varepsilon_0 \varepsilon_2} e^{i\beta x} e^{-k_1 z} \quad (2.13)$$

Where  $A_1$ , and  $A_2$  are unknowns which can be found by applying boundary conditions at  $z=0$ . Finally, from boundary conditions and simple algebraic manipulation one can reach to central result of dispersion relation of SPP propagating in x-direction as

$$\beta = k_0 \sqrt{\frac{\varepsilon_1 \varepsilon_2}{\varepsilon_1 + \varepsilon_2}} \quad (2.14)$$

Now one can do similar manipulation for TE solutions and finally can come to conclusion that no TE solutions are available for SPPs. Thus concluding that these waves are strictly TM waves in single MD interface.

Figure 2.3 shows the dispersion relation plot, normalized wave vector vs normalized frequency with respect to Plasmonic frequency  $\omega_p$ . Plot is for gold described by real Drude dielectric function and quartz ( $n=1.44$ ) interface. Solid curves show the real part of normalized  $\beta$  while dashed line shows imaginary part. SPP excitation corresponds to right of the light line and are bounded in nature. Radiation region in the metal is the left of light line for  $\omega > \omega_p$ , which is transparency region. Light line is defined as  $\omega = \beta_0 c$ , where  $\beta_0$  is free space propagation constant, and  $c$  is speed of light. Also, dispersion curve of SPP lies on the right of light line, thus SPP has shorter wavelength than free space propagating waves. In between radiation and bounded region there is prohibited region for propagation where  $\beta$  is purely imaginary. Thus SPPs are strongly bounded hybrid kind of waves, bound on interface between metal and dielectric. These waves are in addition evanescent fields in longitudinal direction to propagation and are strictly TM polarized waves in case of MD interface.

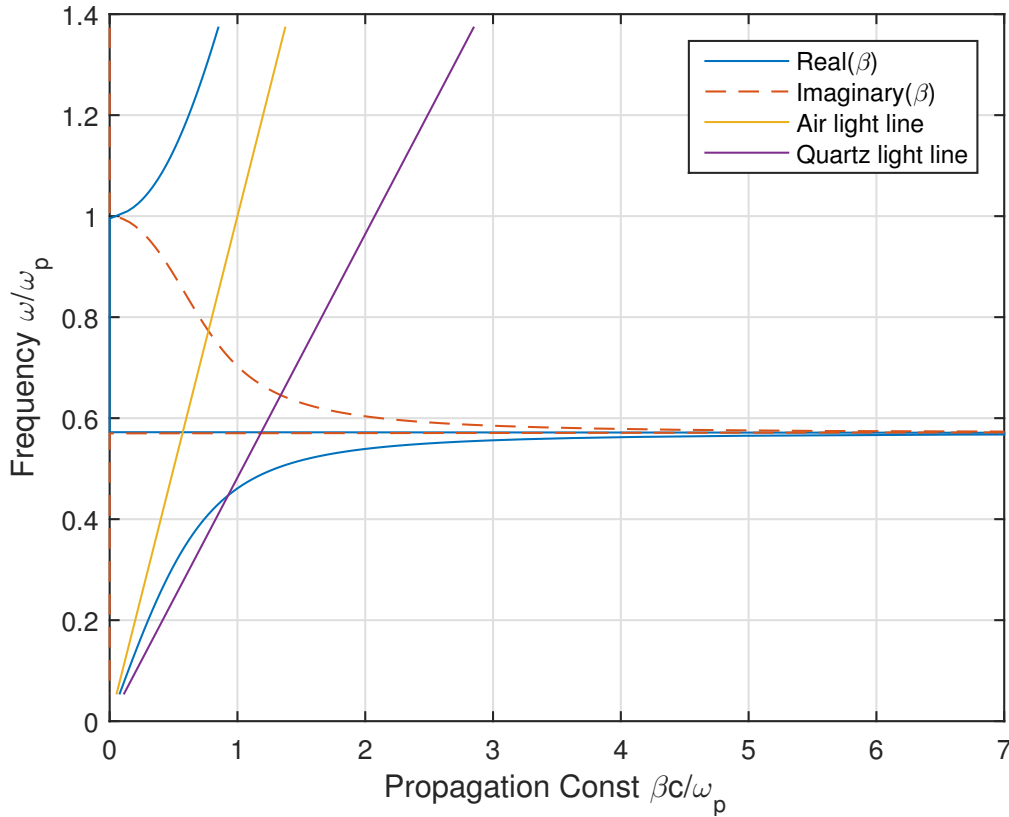


Figure 2.3: Dispersion relation of SPP at MD interface, with gold and quartz

Since the basic idea and characteristics of SPPs have been discussed, now we briefly introduce multilayer systems such as metal-dielectric-metal (MDM) or dielectric-metal-dielectric (DMD). In MDM or DMD each interface supports bounded SPPs which are coupled to each other if the separation between these interfaces are such that the evanescent tails in sandwiched media meets. One can think of these MDM or DMD as two single layered MD interfaces coupled together. Figure 2.4 shows geometry of such system where in the case of MDM layer 1 is dielectric sandwiched between metal layers 2 and 3, or in case of DMD layer 1 is metal sandwiched between layer 2 and 3 dielectric. Now by applying Maxwell's equation to reach to wave equation and then by applying boundary conditions similar to single layer system one can derive

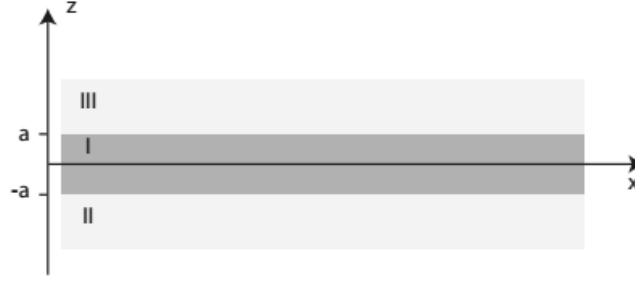


Figure 2.4: Geometry of three layered system (MDM or DMD) where layer 1 (metal or dielectric) is sandwiched between two semi-infinite media (dielectric or metal)

dispersion relation for these multilayer systems and is given as follow

$$\tanh(k_1 a) = -\frac{k_2 \varepsilon_1}{k_1 \varepsilon_2} \quad (2.15)$$

$$\coth(k_1 a) = -\frac{k_2 \varepsilon_1}{k_1 \varepsilon_2} \quad (2.16)$$

Equation 2.15 shows modes of odd parity where  $E_x(z)$  is odd,  $H_y(z)$  and  $E_z(z)$  are even functions while equation 2.16 shows modes of even parity with  $E_x(z)$  is even,  $H_y(z)$  and  $E_z(z)$  are odd functions. Figure 2.5 is visualization of these odd and even parity modes in multilayer systems such as MDM.

## 2.4 TWTLs

Since we gave basic idea about behavior of SPs on metal-dielectric interface, in this section we will discuss modes in Two Wire Transmission Line (TWTL). It is necessary to study the behavior of TWTL because our plasmonic nanoantenna is based on TWTL flared at one end. In order to analyze the behavior of nanoantenna, we need to excite the right mode in TWTL. Two Wire Transmission Line (TWTL) is the extension of plasmonic gap waveguides [Veronis and Fan, 2007], where metals has finite thickness and width, and are much smaller than wavelength of interest.

We simulated TWTL within homogeneous and on interface of heterogeneous media, using COMSOL MULTIPHYSICS. We used modal analysis module of COMSOL

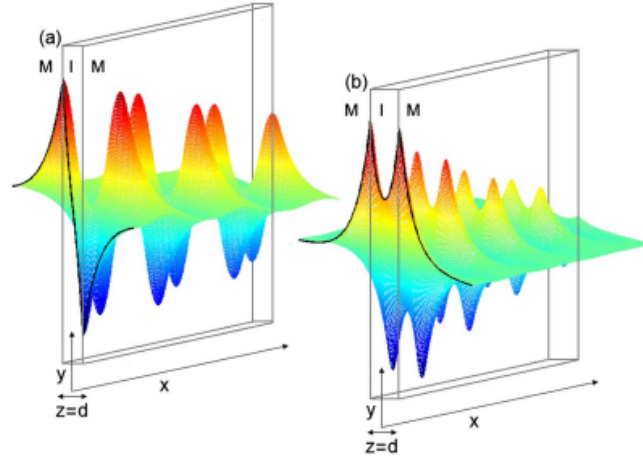


Figure 2.5: Mode profile of a) odd parity SPPs and b) even parity SPPs for MDM structure [Dionne et al., 2006]

for finding eigen value of modes. We use same geometrical parameters for TWTL as we used for plasmonic horn nanoantenna. Width  $b$  of metallic wire is 100 nm, gap  $g$  between two wires is 30 nm, and thickness  $c$  is 50 nm. We used same materials i.e silver (Ag) and quartz in homogeneous case, and silver (Ag), quartz (substrate), and air(cladding) in heterogeneous case. TWTL supports two basic bound propagating modes; asymmetric, and symmetric. Figure 2.6 shows mode profile for TWTL inside homogeneous medium, quartz, in which Figure 2.6a shows  $|E|$  profile of asymmetric mode, while Figure 2.6b shows mode profile of symmetric mode. Similarly,  $|H|$  field is also shown in Figure 2.6c and 2.6d. It can be seen that symmetric mode are loosely bounded, while asymmetric modes are tightly bounded and have strong field distribution.

We also observed that the effective index ( $n_{eff}$ ), complex quantity, for symmetric mode is smaller than asymmetric mode, which means that propagation length  $L_p$  of symmetric mode is higher than asymmetric mode. The real part of  $n_{eff}$  is related to propagation loss or attenuation constant  $\alpha$  and imaginary part is related to propagation constant  $\beta$  of complex propagation constant or wave number. Propagation

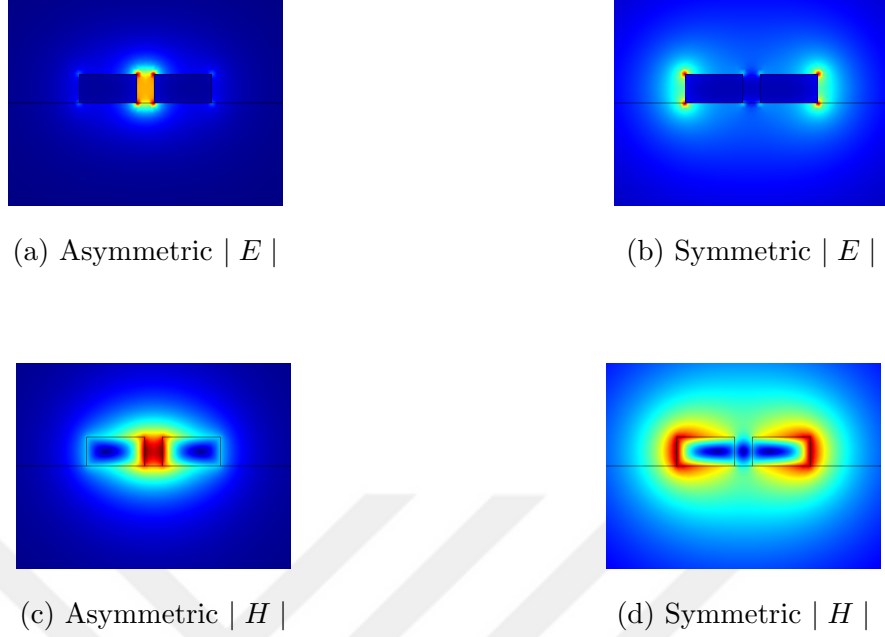


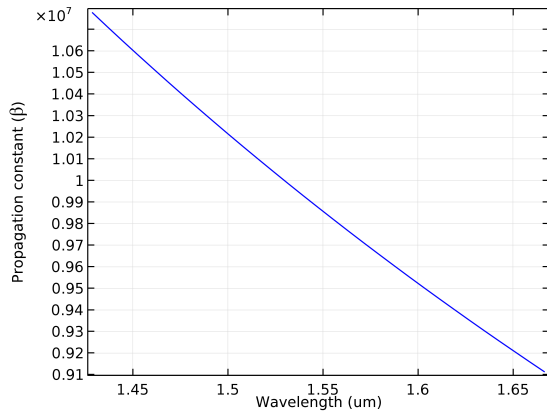
Figure 2.6: Mode profile of TWTL in homogeneous media (quartz) at  $1.55 \mu\text{m}$  wavelength.

length  $L_p$  is length after which power decays by  $1/e$  of its initial value, and is given as

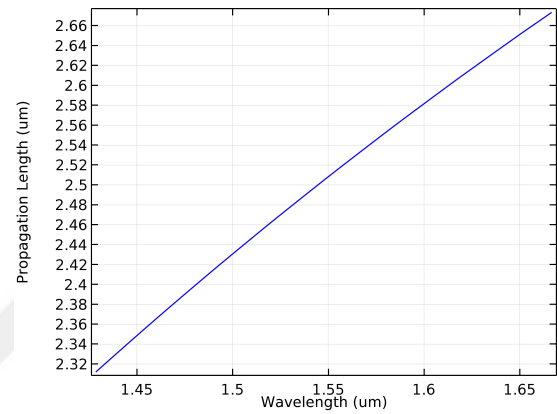
$$L_p = \frac{\lambda_0}{4\pi \text{real}\{n_{eff}\}} \quad (2.17)$$

We are interested in asymmetric modes for our plasmonic horn nanoantenna application, therefore, we further analyze asymmetric mode as a function of wavelength for both homogeneous and heterogeneous case. Figure 2.7 shows dispersion relation and propagation length for homogeneous and heterogeneous medium case. Figure 2.7a and 2.7c shows propagation constant  $\beta$  for homogeneous and heterogeneous case respectively. It can be seen that propagation constant for homogeneous case is greater than heterogeneous, which means that fields are tightly bounded in homogeneous case inside the gap. However, from Figure 2.7b and 2.7d, which shows propagation length for homogeneous and heterogeneous case respectively, it can be seen that propagation length for heterogeneous case is greater than homogeneous case. Thus in the case of

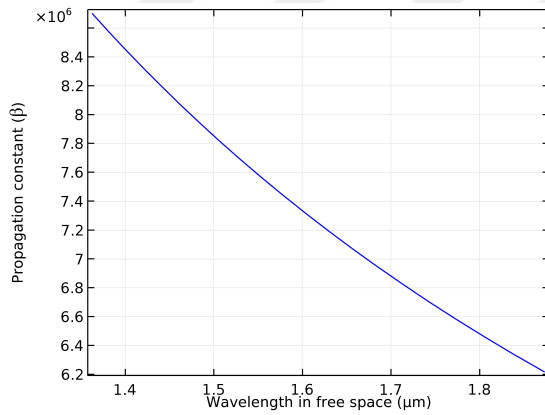
heterogeneous, the power will propagate more as compare to homogeneous medium case.



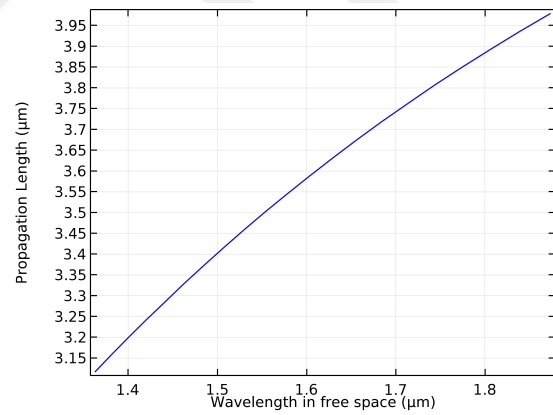
(a) Propagation constant ( $\beta$ ) in homogeneous medium



(b) Propagation Length  $L_p$  in homogeneous medium



(c) Propagation constant ( $\beta$ ) in heterogeneous medium



(d) Propagation Length  $L_p$  in heterogeneous medium

Figure 2.7: Propagation constant  $\beta$ , and Propagation Length  $L_p$  for TWTL in homogeneous and heterogeneous media

## 2.5 Basic definitions of Antenna theory

In this section we introduce some basic definitions related to antenna theory, which we used throughout the whole thesis.

### 2.5.1 Radiation pattern

A mathematical or geographical representation of antennas' radiation properties, determined in far-field region, as function of spacial coordinates (usually spherical) is known as radiation pattern of antenna. Radiation properties include: power pattern, field pattern, directivity or polarization. Figure 2.8 shows the power pattern of antenna as function of spherical coordinate system, where  $r$  represents magnitude,  $\theta$  represents elevation angle, and  $\phi$  represents azimuth angle. Radiation pattern of antenna consists of major lobe, and minor lobes as shown in the figure.

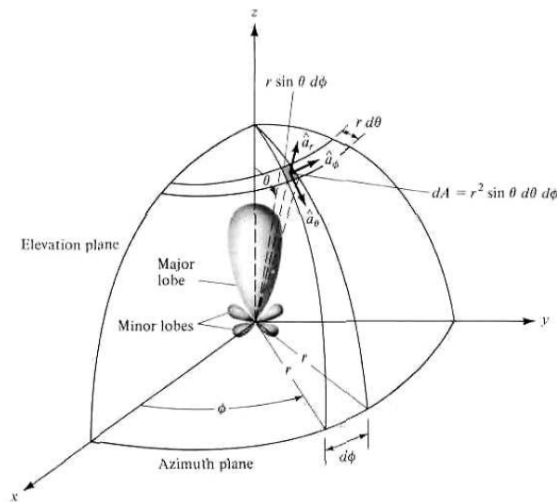


Figure 2.8: Radiation pattern (power pattern) in coordinate system [Balanis, 2016].

### 2.5.2 Directivity

Directivity is one of the important merit in antenna design and analysis, with which antennas' operations are judged. Directivity  $D(\theta, \phi)$  is defined as the ratio of angular

radiation intensity ( $p(\theta, \phi)$ ) in given direction to the total radiation intensity in all directions ( $P_{rad}$ ), and is given as follow

$$D(\theta, \phi) = 4\pi \frac{p(\theta, \phi)}{P_{rad}} \quad (2.18)$$

Where  $\theta$ , and  $\phi$  are elevation and azimuth angles, respectively.

### 2.5.3 Principal patterns, E-plane and H-plane

Radiation patterns are often represented in-terms of the plane in which E-field of H-field lies. These planes are only defined for antennas which radiates with linear polarization. E-plane is plane in which electric field vector and maximum radiation direction lies. On other hand, H-plane represents a plane in which magnetic field vector and maximum radiation direction lies.

### 2.5.4 Reflection coefficient

Another important figure of merit used to characterize antennas' operation is reflection coefficient, or often known as amplitude reflection coefficient. It is a parameter which quantize how much of electromagnetic wave or power is reflected from an interface between two different mediums with different impedances. It is defined as the ratio of amplitude of reflected wave to incident wave. Amplitude reflection coefficient is given as

$$\Gamma = E^- / E^+ \quad (2.19)$$

Where as  $E^-$  is amplitude of reflected wave, and  $E^+$  is amplitude of incident wave.

## Chapter 3

### PLASMONIC HORN NANOANTENNA

#### 3.1 Antenna structure

Basic structure of plasmonic horn nanoantenna comprises of Silver-air-Silver (Ag-air-Ag) or Two Wire Transmission Line (TWTL) (or slot waveguide) flared in one axis, as shown in the figure 3.1. Radiator portion (flared section) has length  $l$ , flaring angle  $\theta$ , and width at the end of radiator  $t$ . While, TWTL section of the nanoantenna have length  $a$ , width  $b$ , and gap  $g$  between the two silver wires. Thickness of metal (or the antenna) is given by  $c$ . Parameters  $a$ ,  $b$ ,  $c$ , and  $g$  are kept constant for all the analysis, and are equal to 1000 nm, 100 nm, 50nm, and 30nm respectively.

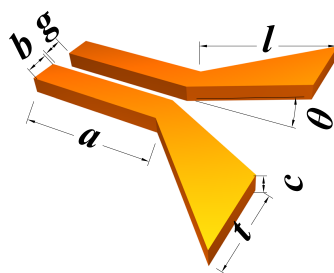


Figure 3.1: Schematics of plasmonic sectoral horn antenna.

#### 3.2 Simulation setup

For complex plasmonic waveguide and antenna geometry, numerical analysis should be carried out, since analytical solutions are only available for basic waveguide ge-

ometries such as MI, MIM, and IMI or antennas such as dipole. In literature, for plasmonic horn nanoantenna, along with TWTL, methods such as Finite Element Method (FEM) [Ramaccia et al., 2011], and Finite Difference Time Domain (FDTD) [Yang et al., 2014, Yang et al., 2016] are used. For all simulations and analysis, we base our choice of using FEM on the fact that, while using FDTD method, plasmonic structures requires mesh size as small as 0.5nm to perform accurate simulation [Taflove, 2000], which increases time and memory required for simulation. All the simulations were carried out in FEM based software, COMSOL MULTIPHYSICS.

### 3.2.1 Selection of Physics and Study Steps

For computation of electromagnetic fields, and time harmonic wave equation in our high frequency system, we used “Electromagnetic Waves, Frequency domain (emw)” as physics interface under “Radio Frequency” interface. For study steps, we used “Boundary Mode Analysis” and “Frequency Domain”. Boundary Mode Analysis is used to compute propagation constant and mode for TWTL waveguide, which we will subject to the horn nanoantenna structure in Frequency Domain study.

### 3.2.2 Geometry

We simulated horn nanoantenna in different cases: inside homogeneous medium, on the interface of two different media (heterogeneous), and with ground plane (see subsequent sections for details). The basic antenna geometry was same for all cases, although we changed length  $l$  of radiating flare in order to shift the central resonance to  $1.55 \mu\text{m}$ .

Geometry of the nanoantenna was drawn with 2-D “Polygon” feature under “Work Plane” tree as shown in the Figure 3.2. Afterwards, this 2-D structure was extended to 3-D by using “Extrude” function under “Geometry” tree, and was converted to solid using “Convert to Solid” feature. Complete 3-D structure is shown in Figure 3.3.

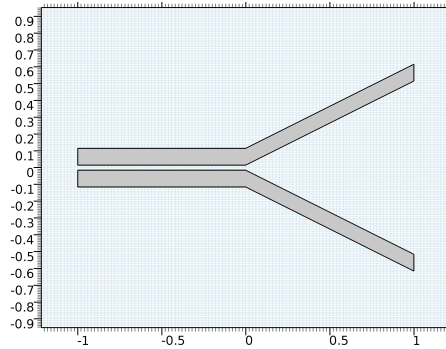


Figure 3.2: Basic 2-D Structure of plasmonic horn nanoantenna using Polygon feature.

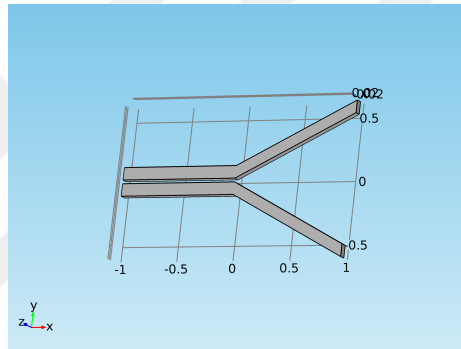


Figure 3.3: 3-D finalized structure of plasmonic horn nanoantenna after using “Extrude” and “Convert to Solid” features.

### 3.2.3 Boundary Conditions

For termination of simulation domain Cartesian Perfect Matching Layer (PML) was used as boundary condition. Plasmonic horn nanoantenna was enclosed inside a cube, with PML layer at each side of the cube as shown in Figure 3.4.

### 3.2.4 Materials

For simulations we used mainly three types of material: glass ( $n=1.44$ ), air ( $n=1$ ) as cladding, and silver. Permittivity for silver was defined by fitting interpolation to the data obtained from [Johnson and Christy, 1972b]

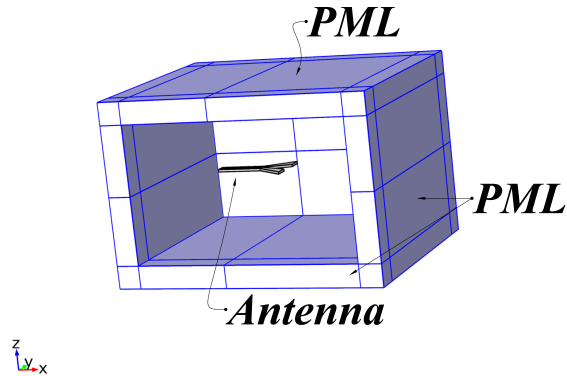


Figure 3.4: Plasmonic horn nanoantenna inside a PML cubic box.

### 3.2.5 Excitation Port

In order to excite whole geometry of the antenna, "Numeric Port" was used, and can be found under the "Study" tree. For this purpose, a rectangular surface was defined at the end of the TWTL as shown in Figure 3.5, and input power of 1 Watt was set. Numeric port determines the propagation constant and mode for TWTL via boundary mode analysis, which was selected as study step.

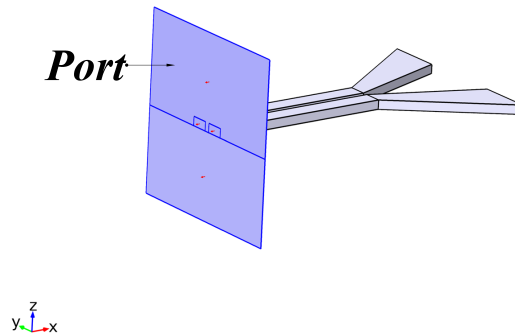


Figure 3.5: Excitation port for plasmonic horn nanoantenna.

### 3.2.6 Mesh

Meshing is the crucial step for any simulation domain as the accuracy, time, and memory depends on meshing . In case of COMSOL, if mesh is too coarse, apart from inaccuracy of results, the simulation does not converge or might take a lot of time in convergence. On other hand, if mesh is too fine, simulation takes more computational time and memory. Ideally, maximum element size of tetrahedral mesh should be less than or equal to  $10^{\text{th}}$  fraction of operating wavelength. However, in our case we are limited by the minimum geometrical parameter used, which is gap  $g$  between to wires of TWTL, and is equal to 30 nm. In order to compute the mode accurately in this gap, one should set the maximum element size as  $g/10$ . Therefore, we used user controlled mesh in which we used fine mesh around gap  $g$  as small as 3 nm, and in material or in domain far from antenna, we found wavelength/5 as optimum element size. For PML, "Swept" mesh was used with fixed number of elements equal to 5. Whole meshed geometry is shown in Figure 3.6.

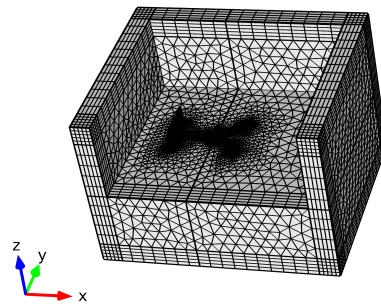


Figure 3.6: Meshing of geometry in COMSOL.

### 3.2.7 Far-field Calculation

Far-field radiation pattern is one of the important merit to analyze operation of antennas. For far-field calculations, we defined a box around the radiating flares, and a small hole was made in the box to exclude the TWTL from the far-field calculation. COMSOL uses Stratton-Chu integration [Stratton, 2007] method for far-field calculations, which basically projects the near-field into far-fields.

### 3.3 Antenna in homogeneous medium

We start our analysis by simulating plasmonic horn nanoantenna enclosed inside glass ( $n=1.44$ ), shown in Figure 3.7. In order to validate our simulation scheme, we replicate results reported in [Yang et al., 2014]. Plasmonic horn nanoantenna was simulated for  $t$  equal to 100nm,  $\theta$  equal to  $26.6^\circ$ . We observe effect on radiation pattern by changing  $l$ .

In order to analyze plasmonic horn nanoantenna and to explore its operational

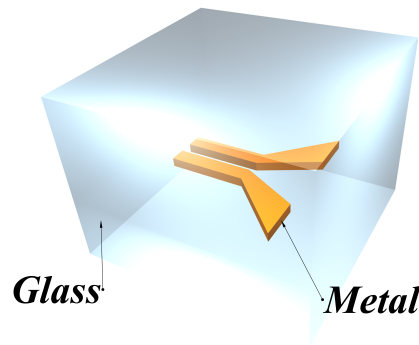


Figure 3.7: Plasmonic horn antenna enclosed in glass.

characteristics, we present results in-terms of 2-D near-field  $E_y$  intensity, far-field directivity pattern, and amplitude reflection coefficient ( $\Gamma$ ). All the near-field plots, and directivity patterns are analyzed for central  $1.55 \mu\text{m}$  wavelength (unless otherwise specified), and amplitude reflection coefficient is analyzed over range of wavelength

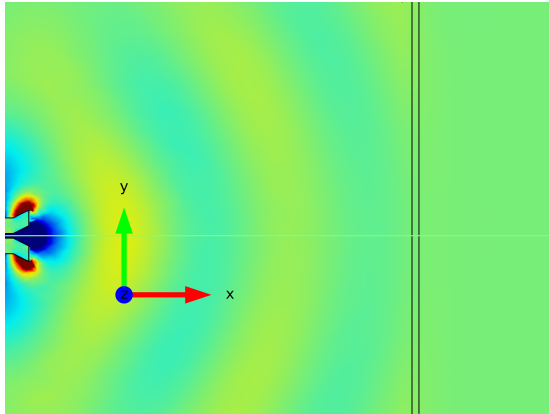
around  $1.55 \mu\text{m}$ . In Figure 3.8, the near-field  $E_y$  intensity shows that flares are acting as impedance matching section between TWTL and glass. As antenna length  $l$  is increased, it can be observed that E-field distribution gradually becomes planar and uniform away from the aperture of the horn antenna, specifically for the case of  $l = 1000\text{nm}$ , E-field distribution is nearly completely uniform. It can be inferred from this analysis that maximum directivity is attained for  $l = 1000\text{nm}$ .

Figure 3.9 shows far-field E-plane and H-plane directivity pattern (in linear scale) for different lengths at  $1.55 \mu\text{m}$  wavelength. For  $l$  equal to  $100\text{nm}$  (Figure 3.9a), directivity is approximately 7 at angle of elevation ( $\theta$ ) equal to 0. Since maximum directivity is in the direction of antenna aperture, thus this antenna can be regarded as end-fire. As we increase  $l$  to  $500\text{nm}$  (Figure 3.9b) and  $1000\text{nm}$  (Figure 3.9c), directivity increases to 12 and 14, respectively. Also, as  $l$  increases, beam-width becomes narrower. However, when  $l$  was further increased beyond certain point, decrease in directivity was observed, as can be seen from Figure 3.9d. All these results confirm with [Yang et al., 2014], thus this analysis validates our simulation setup.

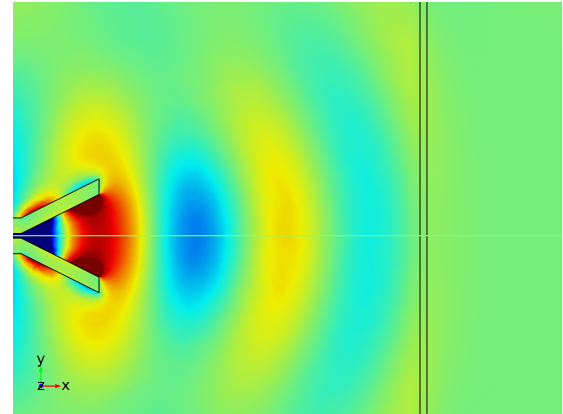
Amplitude reflection coefficient  $\Gamma$  or  $S_{11}$  (hereafter will be used interchangeably), in linear scale, for plasmonic horn nanoantenna with length  $l = 1000\text{nm}$  is given in Figure 3.10. Plasmonic horn has  $S_{11}$  less than 0.14, which shows good impedance matching between TWTL and horn.

### 3.4 Antenna on interface between heterogeneous media (Air and Glass)

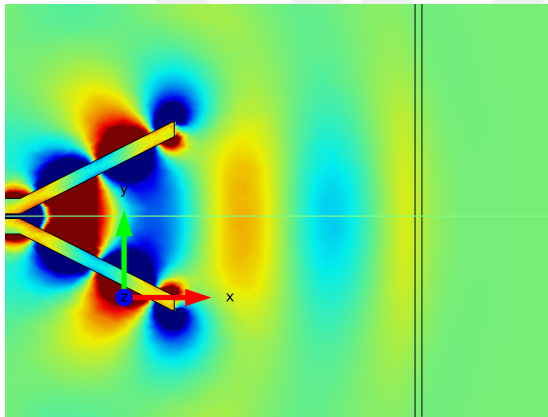
In this section, we analyze plasmonic horn nanoantenna placed on interface between two different semi-infinite media, glass ( $n = 1.44$ ) as substrate and air ( $n = 1$ ) as cladding, as shown in Figure 3.11. Experimentally, nanoantenna or plasmonic devices are fabricated over substrate, which act as support for devices. For instance, glass is used as substrate, which has thickness of  $10^2$  as compared to thickness of plasmonic devices, thus can be taken as semi-infinite. However, the change in refractive index  $n$  between substrate and cladding has drastic effect on nanoantenna radiation and



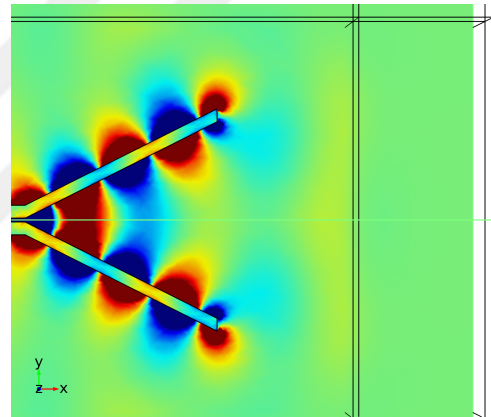
(a) 2-D near-field  $E_y$  intensity plot in XY-plane for  $l = 100\text{nm}$



(b) 2-D near-field  $E_y$  intensity plot in XY-plane for  $l = 500\text{nm}$



(c) 2-D near-field  $E_y$  intensity plot in XY-plane for  $l = 1000\text{nm}$



(d) 2-D near-field  $E_y$  intensity plot in XY-plane for  $l = 1500\text{nm}$

Figure 3.8: Plasmonic horn antenna near-field  $E_y$  intensity plots for  $t = 100\text{nm}$ ,  $\theta = 26.6^\circ$ , and different specified  $l$ .

resonance [Curto et al., 2010, G. et al., 2011].

Results for plasmonic horn nanoantenna on glass substrate are given in Figure 3.12 and Figure 3.13. Figure 3.12a and 3.12b shows top view and side view of 2-D near field  $E_y$  intensities, respectively. It can be observed from Figure 3.12a that

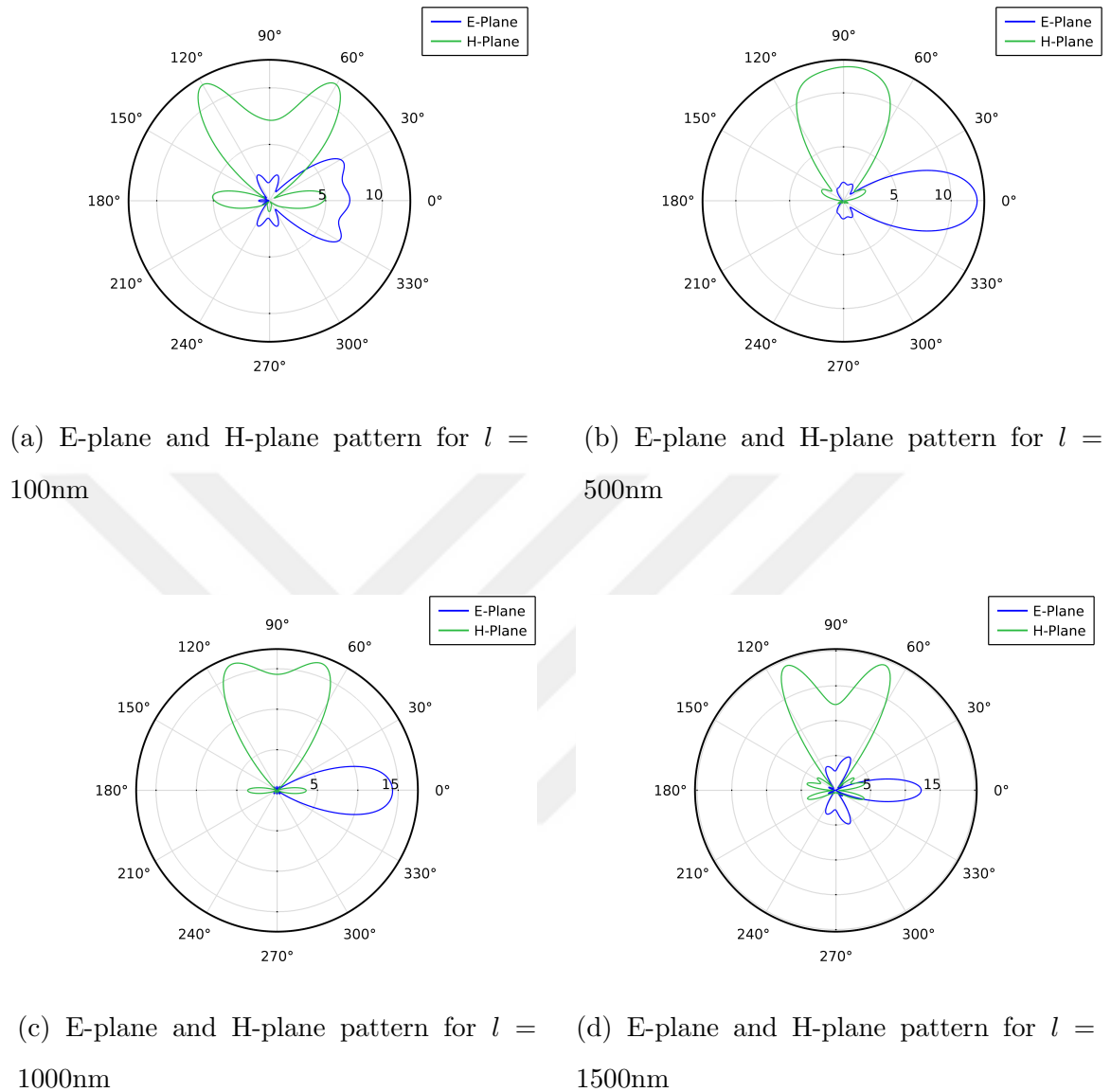


Figure 3.9: Plasmonic horn antenna directivity for  $t = 100\text{nm}$ ,  $\theta = 26.6^\circ$ , and different specified  $l$ .

horn is providing gradual matching between TWTL and surrounding materials, while from Figure 3.12b, once can observe that most of the radiation is directed into the substrate. Since glass has higher refractive index than air, thus antenna radiates more power into the substrate with radiation angle  $\theta = 129^\circ$ . Figure 3.12c shows

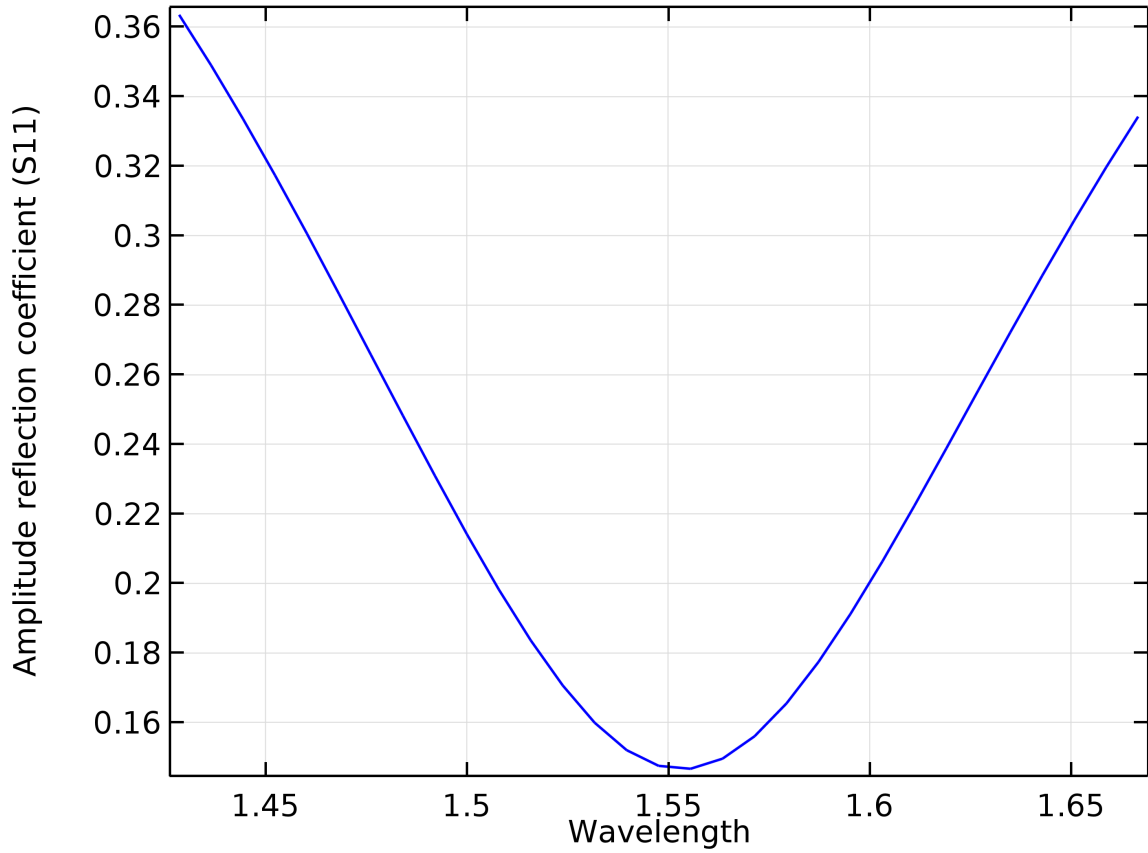


Figure 3.10: Amplitude reflection coefficient ( $S_{11}$ ) of plasmonic horn nanoantenna with  $l = 1000\text{nm}$ .

H-plane directivity pattern where main lobe is directed into substrate with maximum directivity of 14.5 at  $\theta = 129^\circ$ . Finally, Figure 3.12d shows amplitude reflection coefficient of horn nanoantenna. Due to change of substrate, as compared to previous analysis of homogeneous substrate, the effective length of flare also changed, thus shifting the central wavelength (at which  $\Gamma$  is minimum) to higher wavelengths. In order to accumulate for this change, the length  $l$  was decreased to 650nm. At central wavelength of  $1.55 \mu\text{m}$ , amplitude reflection coefficient  $\Gamma$  is equal to 0.09.

In order to further support our argument, we also calculated radiation efficiency defined as  $P_{rad}/P_{in}$  by the nanoantenna in substrate, superstrate, and in all domains,

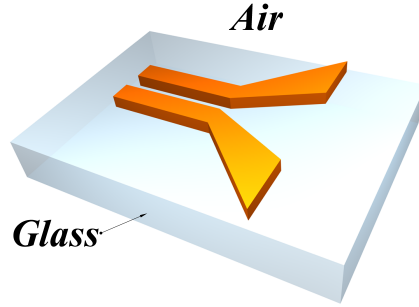


Figure 3.11: Plasmonic horn nanoantenna on glass substrate with  $l = 650\text{nm}$ ,  $t = 300\text{nm}$ , and  $\theta = 20^\circ$ .

where  $P_{rad}$  is radiated power by the antenna, and  $P_{in}$  is input power which 1 Watt. Figure 3.13 shows: total radiation efficiency, radiation efficiency in substrate, and radiation efficiency in air. Total efficiency by antenna is 0.45 at  $1.55\ \mu\text{m}$  wavelength, since it has minimum reflection coefficient at this wavelength. In addition, it can be observed that most of the power is radiated in substrate (red broken-line) as compared to air (blue line). Thus, a fraction of the power can be coupled or extracted from air side or from plane parallel to the antenna, which makes it infeasible for applications such as laser detection or wireless nano-link [Yang et al., 2016], where antenna is required to radiate in broadside or end-fire, respectively.

### 3.5 Antenna on metal-backed ground plane - beam steering

From our analysis in previous section, where antenna was mounted on semi-infinite substrate, we observed that most of the power radiates in to the substrate with refractive index higher than cladding layer. Although plasmonic horn antenna has high directivity, if implemented for wireless nano-link such as reported in [Yang et al., 2016], link performance or efficiency will decrease drastically. Therefore, there is need to devise mechanism with which we can control the radiation of antenna. In this sec-

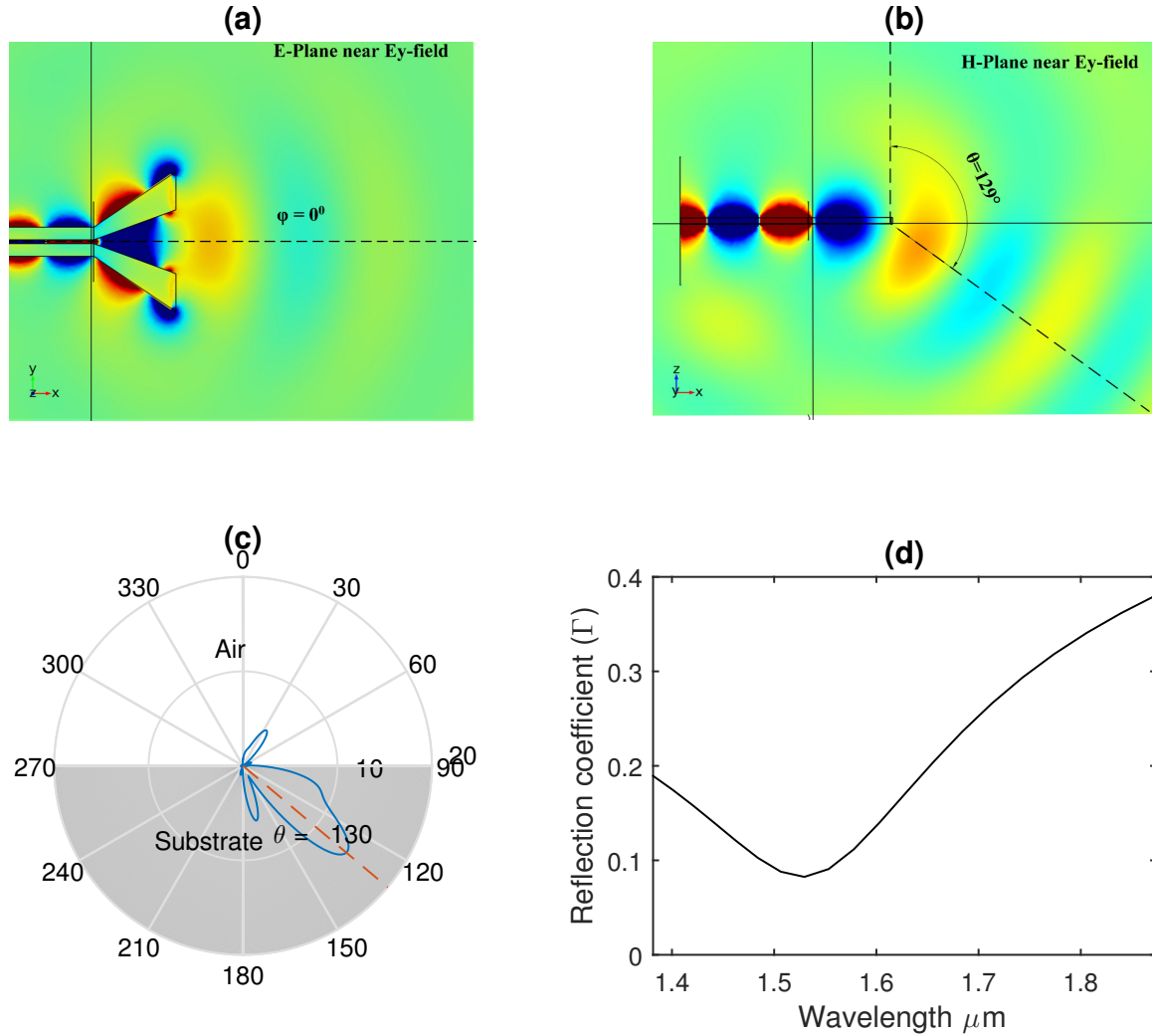


Figure 3.12: Results for plasmonic horn nanoantenna placed over infinite glass substrate. (a) top view of 2-D  $E_y$  field in XY-plane. (b) side view of 2-D  $E_y$  field in XZ-plane. (c) H-plane directivity pattern. (d) Amplitude reflection coefficient  $\Gamma$  in linear scale (black solid-line).

tion, we introduce metallic ground plane on the back of substrate (glass) in order to control the radiation of nanoantenna. If reflecting ground plane is employed below substrate, making substrate thickness finite, the ground plane will act as image antenna [Xi et al., 2013]. The direct emitted light from nanoantenna, and the reflected

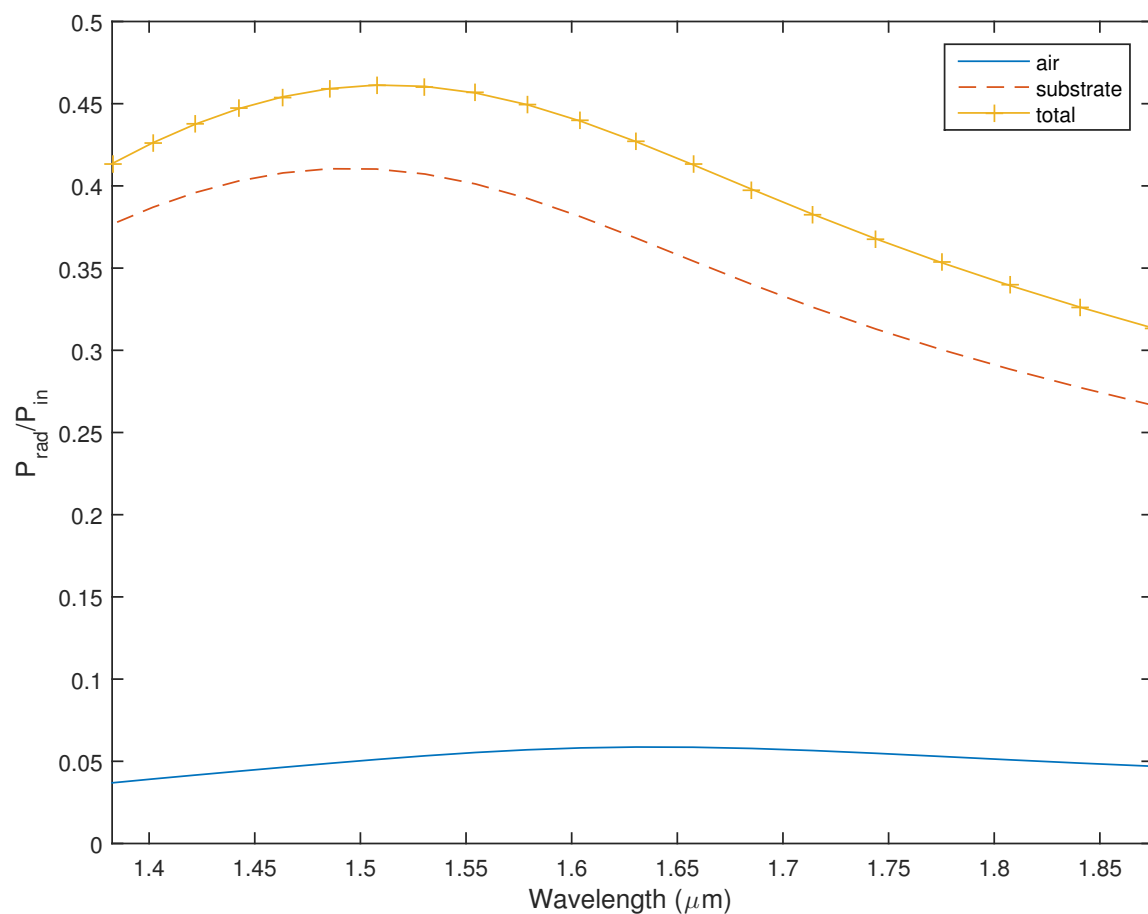


Figure 3.13: Total radiation efficiency (orange +-line), radiation efficiency in substrate (red broken-line), and radiation efficiency in air (blue line).

light from ground plane can interfere with each other with different phases dependent upon the thickness of substrate. This interference shapes the radiation pattern and direction of antenna. In other words, by changing the thickness of substrate, one can control direction of maximum radiation.

Plasmonic horn nanoantenna backed by plasmonic substrate (reflective ground plane-backed substrate) with thickness  $d$  is shown in the Figure 3.14.

Plasmonic horn nanoantenna was simulated for the range of substrate thickness  $d$ , ranging from 200nm to 900nm, and radiation pattern was analyzed at 1.55  $\mu\text{m}$  wavelength. Figure 3.15 shows near-field  $E_y$  plot in XZ-plane, and H-plane directivity

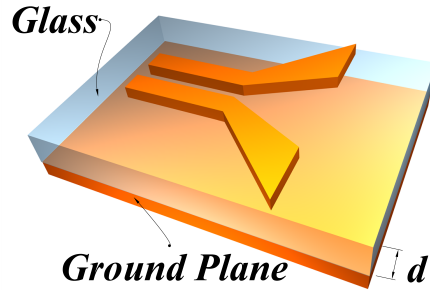


Figure 3.14: Plasmonic horn nanoantenna on metal-backed substrate with substrate thickness  $d$

plot for  $d$  equal to 300nm and 500nm. When  $d$  is equal to 300nm, antenna radiates near broadside with elevation angle  $\theta$  equal to  $28^\circ$  and maximum directivity of 15, as shown in Figure 3.15a and 3.15b. On other hand, when  $d$  is equal to 500nm, nanoantenna radiates near end-fire with  $\theta$  equal to  $79^\circ$ , and maximum directivity of 7. Thus, by proper choice of thickness  $d$  of substrate, one can make end-fire antenna radiate broadside, and vice-versa [Ghadarghadr et al., 2009].

Result for the range of  $d$  is shown in the Figure 3.16, which shows angle of elevation ( $\theta$ ) as function of  $d$ . For the range of 240nm to 450nm, as the thickness increases elevation angle also increases from  $27^\circ$  to  $40^\circ$  gradually, and antenna radiates in air for this whole range. But when  $d$  was further increased above 450nm, elevation angle increases rapidly. For the range of  $d$  equal to 500nm to 650nm, elevation angle changes between  $70^\circ$  to  $80^\circ$  and antenna radiates nearly end-fire. After further increase above 650nm, antenna again radiates broadside (in air). This periodicity was also reported in Figure 12 in [Ghadarghadr et al., 2009], and is due to the fact that ground plane is acting as image antenna, thus both horn nanoantenna and its image can be thought of as two element array. In this case, total radiation pattern is product of element radiation pattern and array factor [Balanis, 2016]. Array factor is exponential function of thickness  $d$  of substrate whose periodicity depends upon the thickness  $d$ , thus we

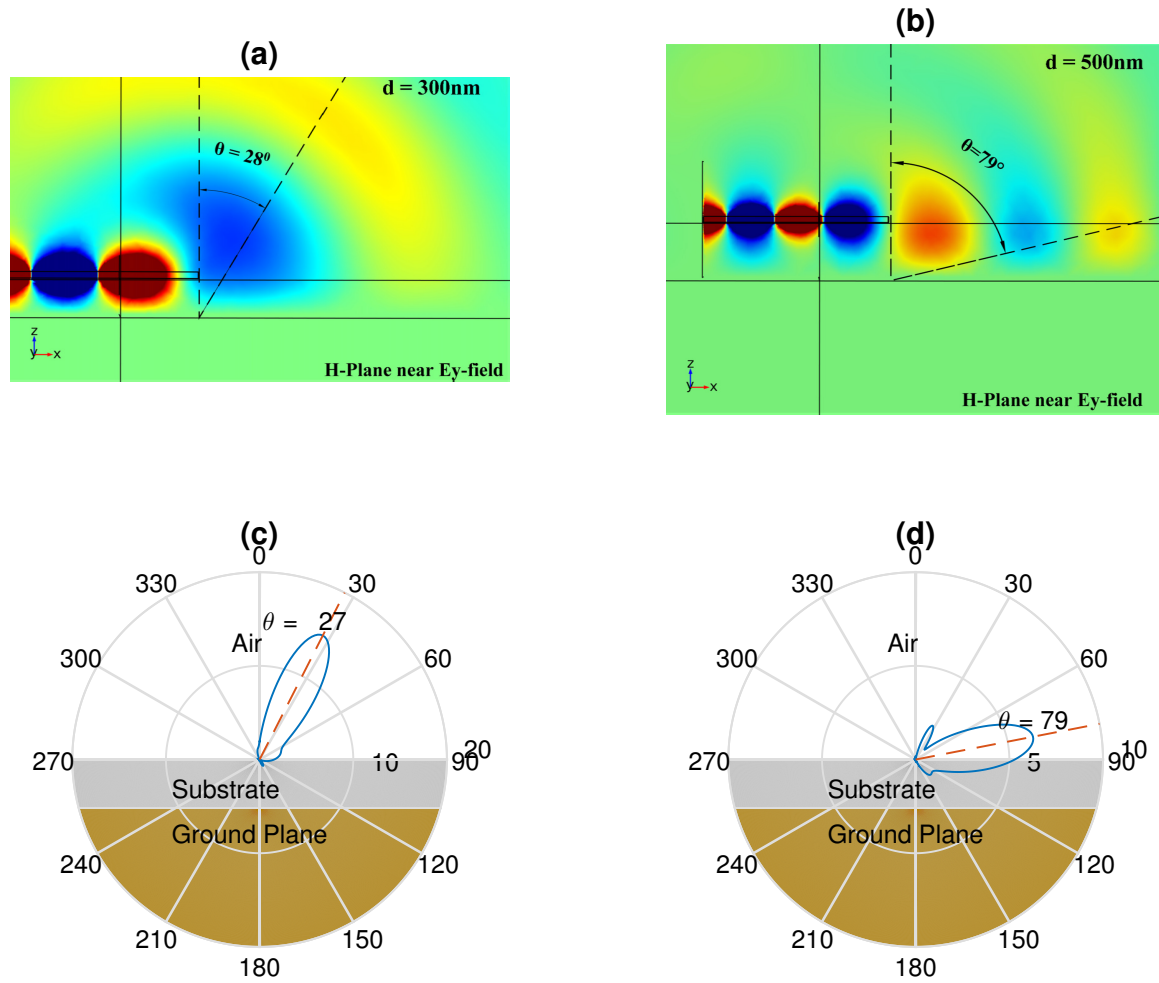


Figure 3.15: (a) Side view of near-field  $E_y$  intensity for  $d = 300\text{nm}$ . (b) Side view of near-field  $E_y$  intensity for  $d = 500\text{nm}$ . (c) H-plane directivity pattern for  $d = 300\text{nm}$ . (d) H-plane directivity pattern for  $d = 500\text{nm}$

observe periodic behavior of antenna.

Finally, we simulated plasmonic horn nanoantenna with ground plane for the range of wavelength to analyze effect of ground plane on reflection coefficient  $\Gamma$  of the nanoantenna with  $d$  equal to  $300\text{nm}$ . Figure 3.17 shows amplitude reflection coefficient, where it can be observed that reflection back in to waveguide from flare is increased and is equal to  $0.1287$ , where previously it was  $0.09$  for the case of semi-

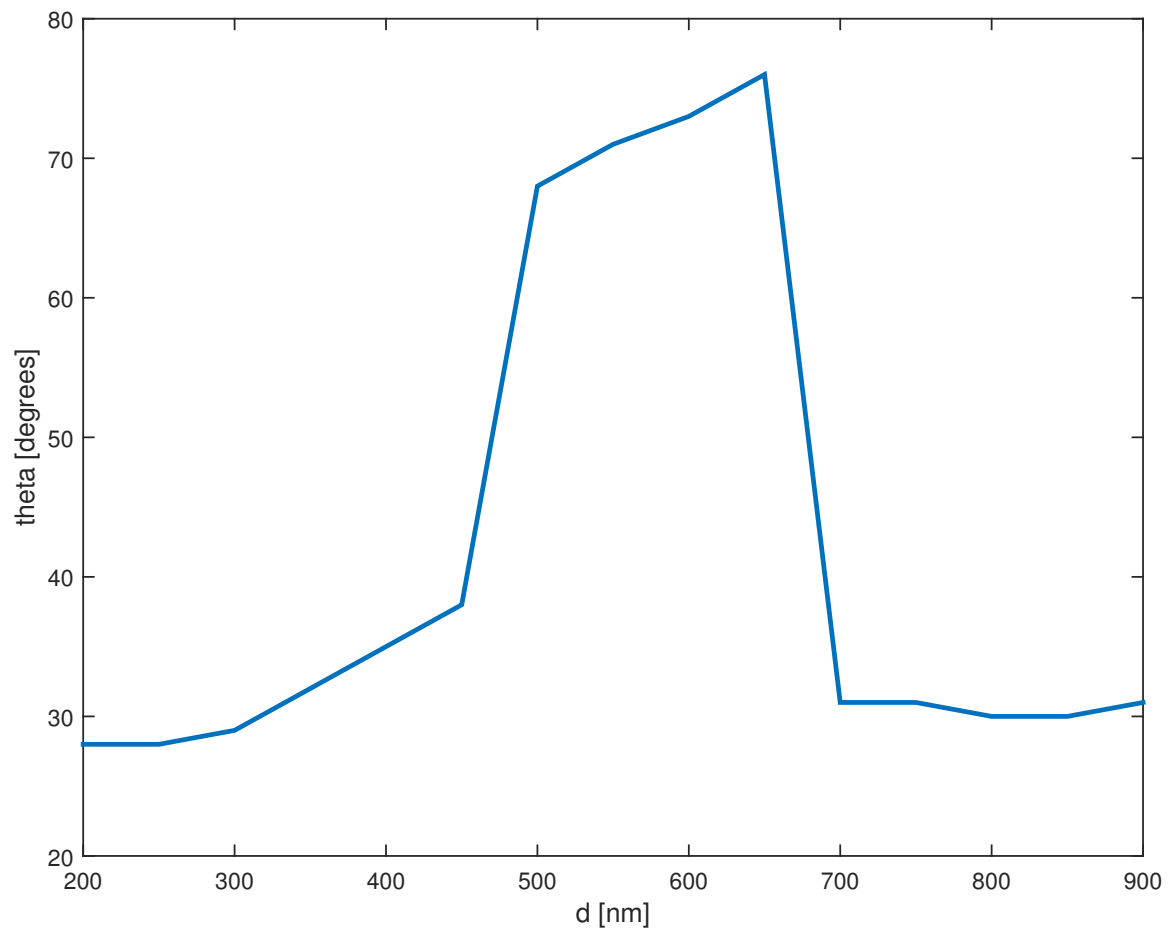


Figure 3.16: Elevation angle  $\theta$  (angle of maximum directivity) as function of thickness  $d$  of substrate.

infinite substrate.

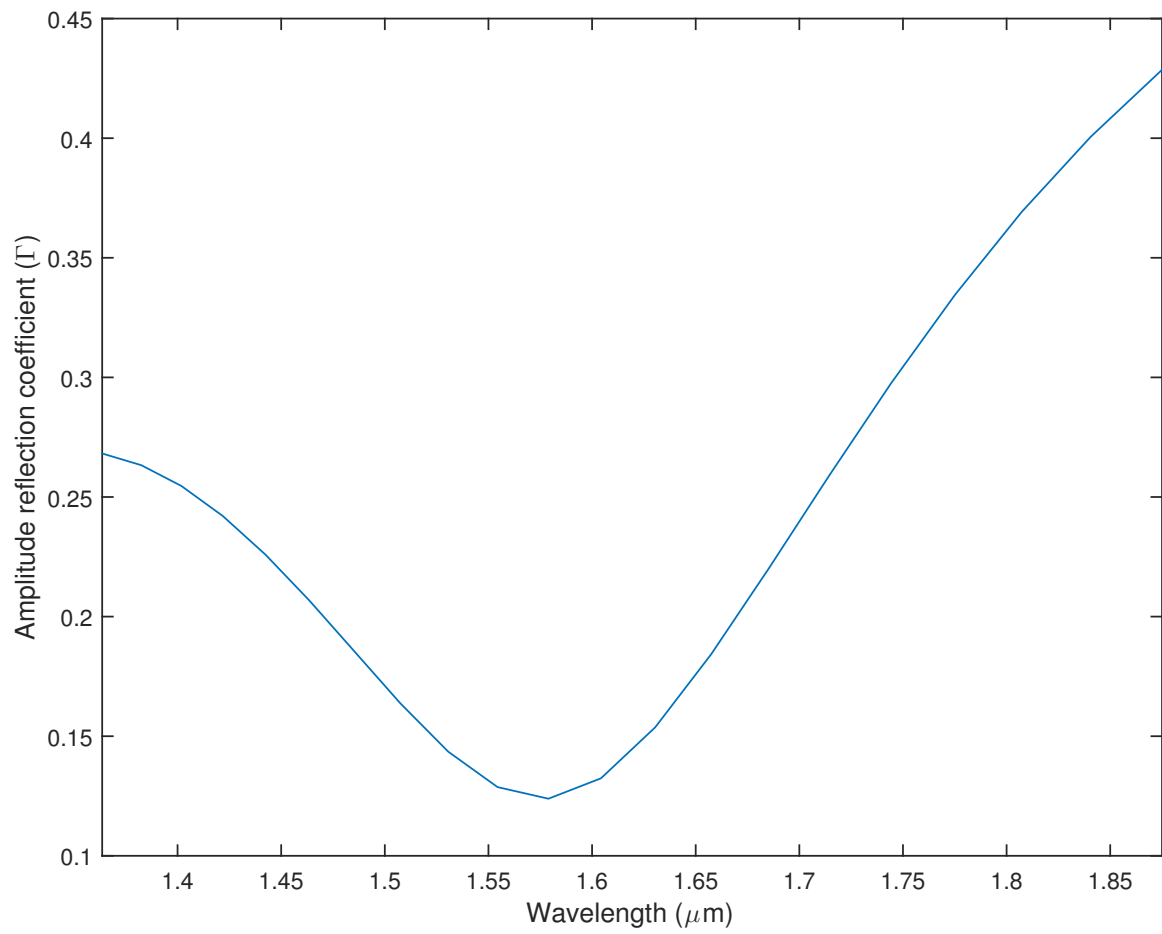


Figure 3.17: Amplitude reflection coefficient of the nanoantenna backed by plasmonic substrate for  $d = 300\text{nm}$ .

## Chapter 4

### IMPEDANCE MATCHING

In previous section, we discussed that for efficient coupling or extraction of power, in a given direction, antenna's maximum radiation should be in the same direction. However, this is not the only factor which determines the efficient coupling (or extraction) of power to the rest of the integrated circuitry which is connected to the nanoantenna. Control of radiation direction ensures efficient coupling (or extracting) of power to the nanoantenna itself, but doesn't not guarantee maximum power transfer to the rest of circuit or transmission lines that guides power. It is known that part of electromagnetic field reflects back from the discontinuity or interface which is perpendicular to its direction of propagation. This reflection depends upon the input impedance which electromagnetic field sees on that specific interface. Thus in order to reduce reflection, if desired, one should match the impedance of the medium in which electromagnetic field is propagating, and input impedance at the interface. This concept of matching is known as impedance matching (IM).

Impedance matching is commonly used in electrical power engineering and in communication engineering, where impedance of an electrical load is matched to the impedance of the power source, in order to ensure maximum power transfer to the load. Same concept is extended to antenna design and transmission line theory, where waveguide or transmission lines are impedance matched to input impedance of antenna using different techniques like quarter wavelength transformation, balun, and conjugate impedance matching, to name a few [Balanis, 2016]. Basic idea of these impedance matching technique is to match known input impedance of load (antenna) to source (transmission line) by introducing an intermediate matching section. In short, input impedance of antenna, and impedance of transmission lines are

important parameters for ensuring efficient matching between antenna and source [Sachkou et al., 2011].

In conventional RF and microwave regime, analytical solution and formulas exist for almost all types of antenna and transmission lines. However, it is not the case for nanoantennas or plasmonic waveguides. Although, in literature, analytical solution or modeling technique for calculating impedance of 2-D and 3-D plasmonic waveguides, such as Metal-Insulator-Metal (MIM) or slot waveguides, have been presented [Xu et al., 2011, Ly-Gagnon et al., 2008, Veronis et al., 2009, Hosseini et al., 2008], but for plasmonic horn nanoantenna, no such study exists. In addition, for slot waveguide or TWTL with metal-backed substrate, as in our case, numerical technique or analytical solution is required to predict its impedance and reflection coefficient  $\Gamma$ .

#### **4.1 Impedance matching**

In this section we employ an impedance matching technique [Xu et al., 2011], by introducing a matching section IM, to match plasmonic nanoantenna with TWTL, as shown in the Figure 4.1. Matching section consists of silver-glass-silver (Ag-glass-Ag) TWTL, with length  $l_2$ , introduced at length  $l_1$  from the flared section. The overall length  $a$  remains same as 1000nm as previous analysis. Thus whole structure of the nanoantenna can be considered as cascaded system of Ag-air-Ag, Ag-glass-Ag, and Ag-air-Ag TWTLs, and flared section. Input impedance of the whole antenna system now depends upon the lengths  $l_1$  and  $l_2$ , and permittivity of dielectric in silver-dielectric-silver section (glass in this case). Thus by choosing appropriate lengths and dielectric material, one can minimize the reflection and control input impedance of the nanoantenna system.

#### **4.2 Analytical model for impedance matching**

In this section we present an analytical model or technique to calculate reflection coefficient for our employed impedance matching technique. In order to minimize the reflection, using impedance Ag-glass-Ag matching section, from the nanonantenna into

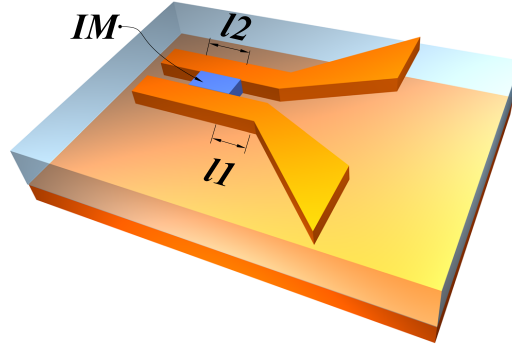


Figure 4.1: Plasmonic horn nanoantenna with impedance matching section (IM) with length  $l_2$  and slot filled with glass (Ag-glass-Ag).

TWTL, one should choose appropriate lengths ( $l_1$  and  $l_2$ ) and dielectric material with permittivity  $\epsilon$ . Since there are no pre-defined formulas to choose these appropriate parameters, one should numerically simulate such structure. In addition, to find out such optimal parameters, to achieve impedance matching, one must do hit and trial simulations, which is time and memory consuming process. Therefore, we developed a three step analytical model which can determine optimal lengths and permittivity of IM section to achieve maximum matching between the nanoantenna and TWTL.

Complete schematic of the analytical model is shown in Figure 4.2. As first step of modeling, we simulated plasmonic horn nanoantenna with Ag-air-Ag TWTL of characteristic impedance  $Z_{0a}$ , as shown in Figure 4.2a, and obtained reflection at interface “B”, given as  $\Gamma(B)$ . Then, we transformed  $\Gamma(B)$ , by arbitrary length  $l_a$ , to interface “A” to obtain reflection coefficient at nanoantenna and TWTL interface, given as  $\Gamma(A)$ . As second step, we simulated cascaded Ag-air-Ag TWTL with characteristic impedance  $Z_{0a}$ , and Ag-dielectric-Ag TWTL with characteristic impedance  $Z_{0d}$ , shown in Figure 4.2b. Similarly, we obtained reflection coefficient at interface “D” from simulation, and transformed it by arbitrary length  $l_b$  of Ag-air-Ag TWTL,



Figure 4.2: Analytical model for impedance matching. (a) Ag-air-Ag TWTL with plasmonic horn. (b) Ag-air-Ag TWTL cascaded with Ag-dielectric-Ag TWTL.

and obtained reflection coefficient at interface “C”, given as  $\Gamma(C)$ . Thus from these two steps, we can have formula for normalized input impedance  $\overline{Z_{od}}$  at interface “C”. Note that  $\varepsilon_0$  is free space permittivity, while  $\varepsilon_d$  is permittivity of dielectric used in Ag-dielectric-Ag TWTL.

Input impedance  $\overline{Z_{od}}$  is given as

$$\overline{Z_{od}} = \frac{Z_{od}}{Z_{oa}} = \frac{1 + \Gamma(D) \exp(2\gamma_a l_b)}{1 - \Gamma(D) \exp(2\gamma_a l_b)} \quad (4.1)$$

Where  $\overline{Z_{od}}$  is normalized impedance of Ag-dielectric-Ag TWTL with respect to impedance  $Z_{oa}$  of Ag-air-Ag TWTL.  $\gamma_a$  is complex propagation constant of Ag-air-Ag TWTL, and  $l_b$  is arbitrary length of Ag-air-Ag TWTL. The third and final step includes calculation, where we cascade the nanoantenna shown in Figure 4.2a to TWTL system shown in Figure 4.2b, and calculate reflection coefficient  $\Gamma(N)$  and normalized input impedance represented as  $\overline{Z_{inN}}$ , at each interface “N”, by the following governing equations

$$\overline{Z_{inN}} = \frac{Z_{inN}}{Z_{0N-1}} = \frac{1 + \Gamma(N-1) \exp(-2\gamma_N l_N)}{1 - \Gamma(N-1) \exp(-2\gamma_N l_N)} \quad (4.2)$$

$$\Gamma(N) = \frac{\overline{Z_{inN}} - \overline{Z_{od}}}{\overline{Z_{inN}} + \overline{Z_{od}}} \quad (4.3)$$

Where  $Z_{inN}$  and  $\Gamma(N)$  are input impedance and reflection coefficient at interface N, and  $\gamma_N$  and  $l_N$  are the complex propagation constant and length of TWTL portion at the end of which N interface lies.

Calculated reflected coefficient for plasmonic nanoantenna with ground plane, with geometrical parameters specified in Section 3.5 and for  $d = 300\text{nm}$ , is shown in Figure 4.3. Figure 4.3 is contour plot of reflection coefficient as function of  $l_1$  and  $l_2$ , calculated at  $1.55\ \mu\text{m}$  wavelength. Ag-glass-Ag is chosen as impedance matching section, and reflection coefficient is calculated by changing lengths  $l_1$  and  $l_2$ . From Figure 4.3, one can determine optimal  $l_1$  and  $l_2$  for impedance matching.

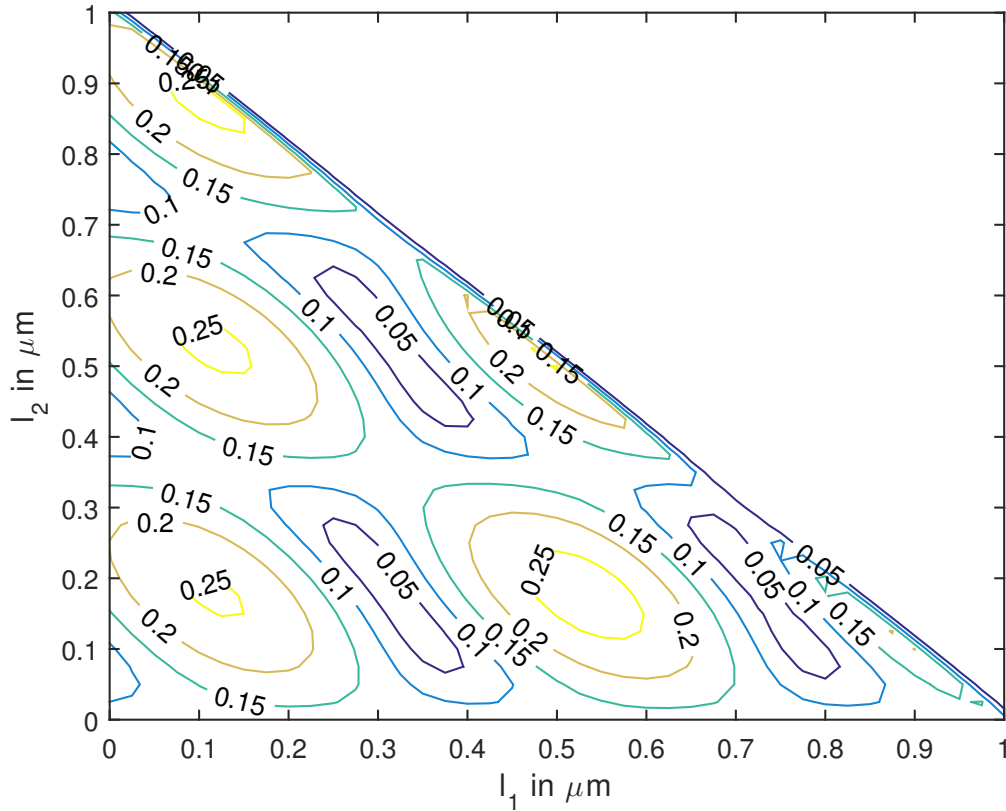


Figure 4.3: Reflection coefficient calculated from analytical model as function of  $l_1$  and  $l_2$ .

### 4.3 Simulation vs. analytical model

In previous section, we proposed analytical model for impedance matching of plasmonic horn nanoantenna with TWTL. In order to validate our model, we selected optimal lengths  $l_1$  and  $l_2$  equal to 350nm and 125nm, respectively, and selected glass as dielectric in Ag-dielectric-Ag impedance matching section. Reflection coefficient is minimum at these lengths, and is equal to 0.0048, according to our analytical model. We simulated geometry with same geometrical parameters, as used in analytical mode, for the range of wavelength around 1.55  $\mu\text{m}$ , and compared results from simulation with analytical model. Figure 4.4 shows reflection coefficient comparison between analytical model and simulation, for impedance matched plasmonic horn nanoantenna, as function of wavelength. Case 1 shows reflection coefficient calculated with analytical model, Case 2 shows simulation result, and for comparison simulated result for plasmonic horn nanoantenna without impedance matching is also plot (Case 3). It can be seen from Figure 4.4, that analytical model agree well with simulated result (Case 1 and Case 2). In addition, impedance matching technique reduced reflection coefficient to 0.038 (simulated result) as compare to 0.128 for the case of antenna without impedance matching (Case 3), at 1.55  $\mu\text{m}$ . Thus presented impedance matching technique improved impedance matching between nanoantenna and TWTL by more than 70%.

In order to further validate analytical model for impedance matching, we took non-optimal lengths  $l_1$ , and  $l_2$  for which we have high reflection coefficient or reflection, and compared it with simulated results for the same lengths. Figure 4.5 shows reflection coefficient for: simulated horn nanoantenna with impedance matching and ground plane, and analytical model, for  $l_1$  equal to 50 nm, and  $l_2$  equal to 100 nm. Reflection coefficient in this case at 1.55  $\mu\text{m}$  wavelength is approximately equal to 0.15, and analytical model is in agreement with simulation result. In addition, we plotted H-plane directivity pattern for metal backed plasmonic horn nanoantenna to observe the effect of impedance matching on directivity, shown in Figure 4.6. Impedance matching has negligible effect on radiation pattern of plasmonic horn nanoantenna.

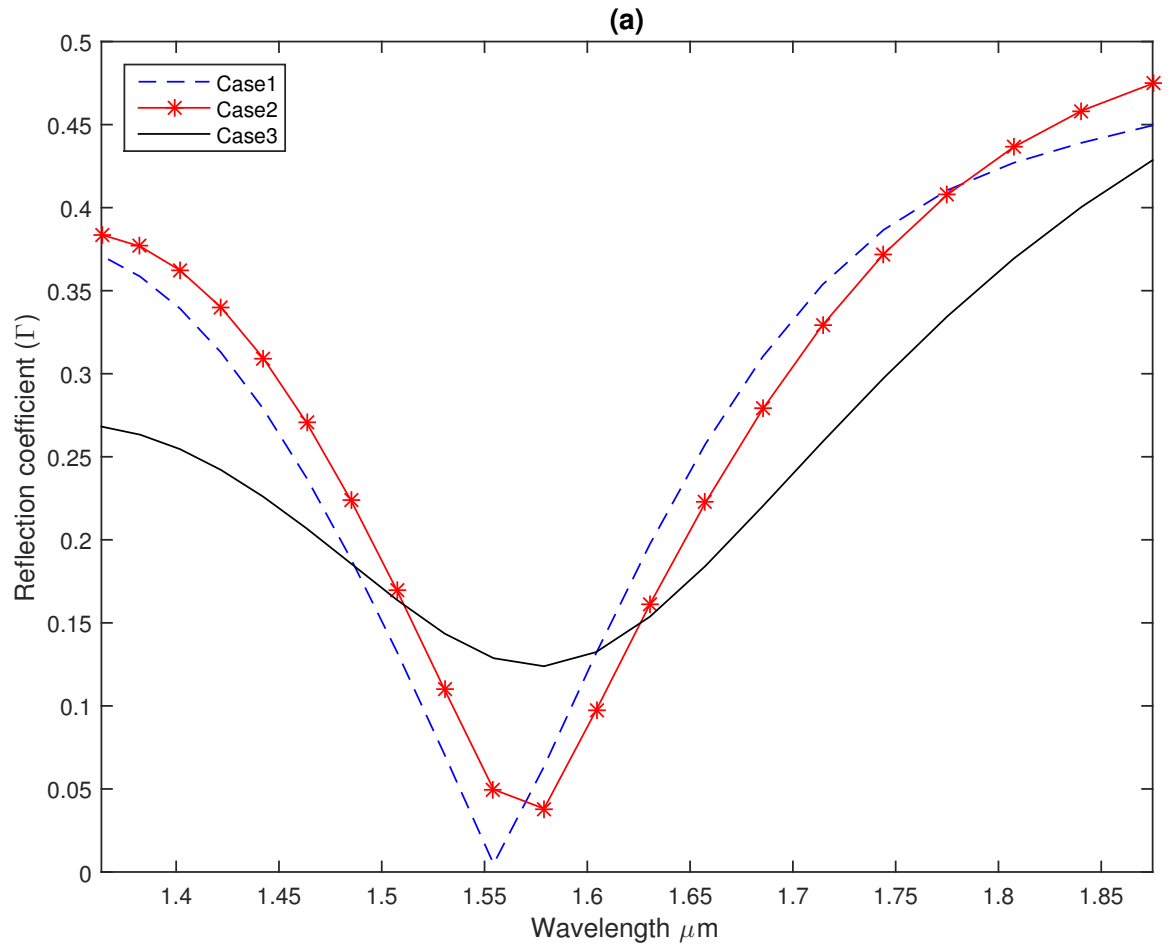


Figure 4.4: Comparison of reflection coefficient of ground-plane backed plasmonic horn antenna with  $l_1 = 350\text{nm}$  and  $l_2 = 125\text{nm}$ ,  $l = 650\text{nm}$ ,  $t = 300\text{nm}$ ,  $\theta = 20^\circ$ , and  $d = 300\text{nm}$ . Case 1 refers to result from analytical model, Case 2 refers to result from simulation, while Case 3 is result for antenna without impedance matching.

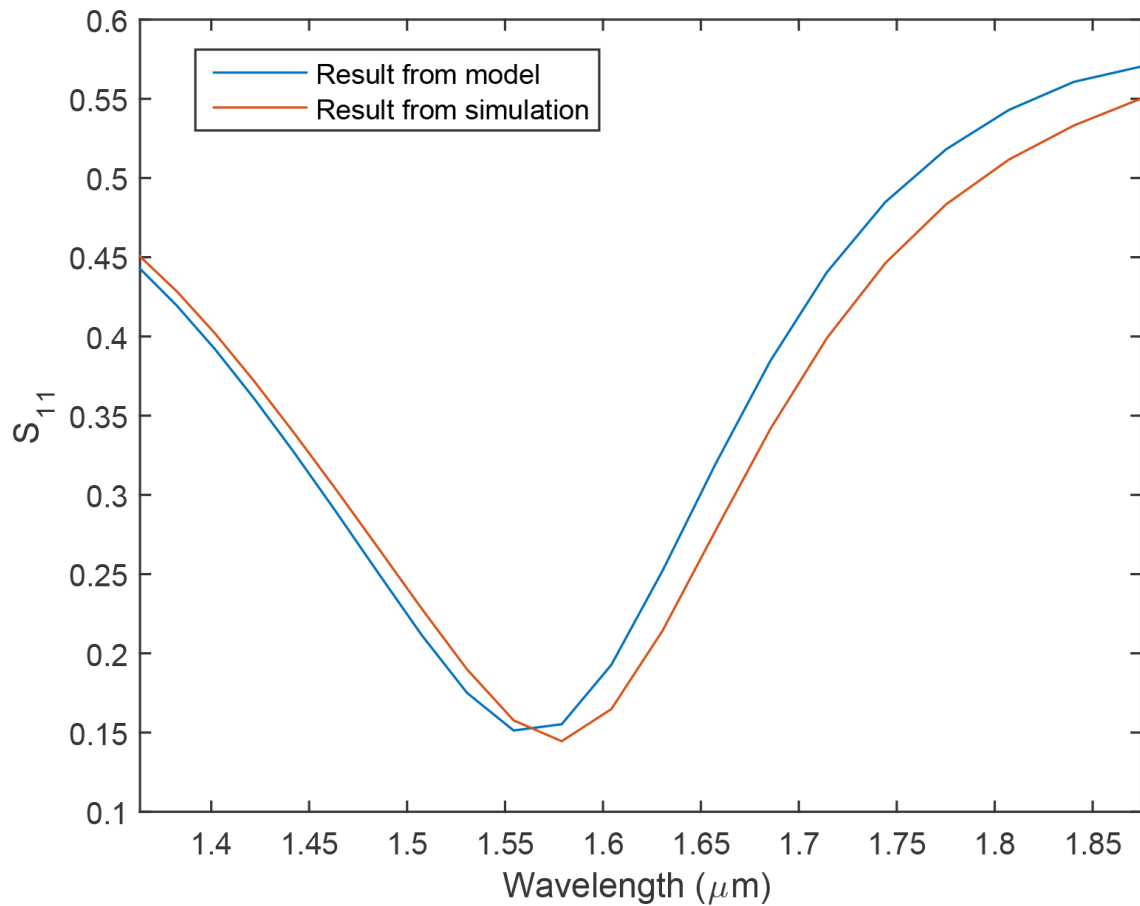


Figure 4.5: Comparison of reflection coefficient of ground-plane backed plasmonic horn antenna with  $l_1 = 50$  nm and  $l_2 = 100$  nm,  $l = 650$  nm,  $t = 300$  nm,  $\theta = 20^\circ$ , and  $d = 300$  nm. Blue line shows result from analytical model, while red line shows result from simulation.

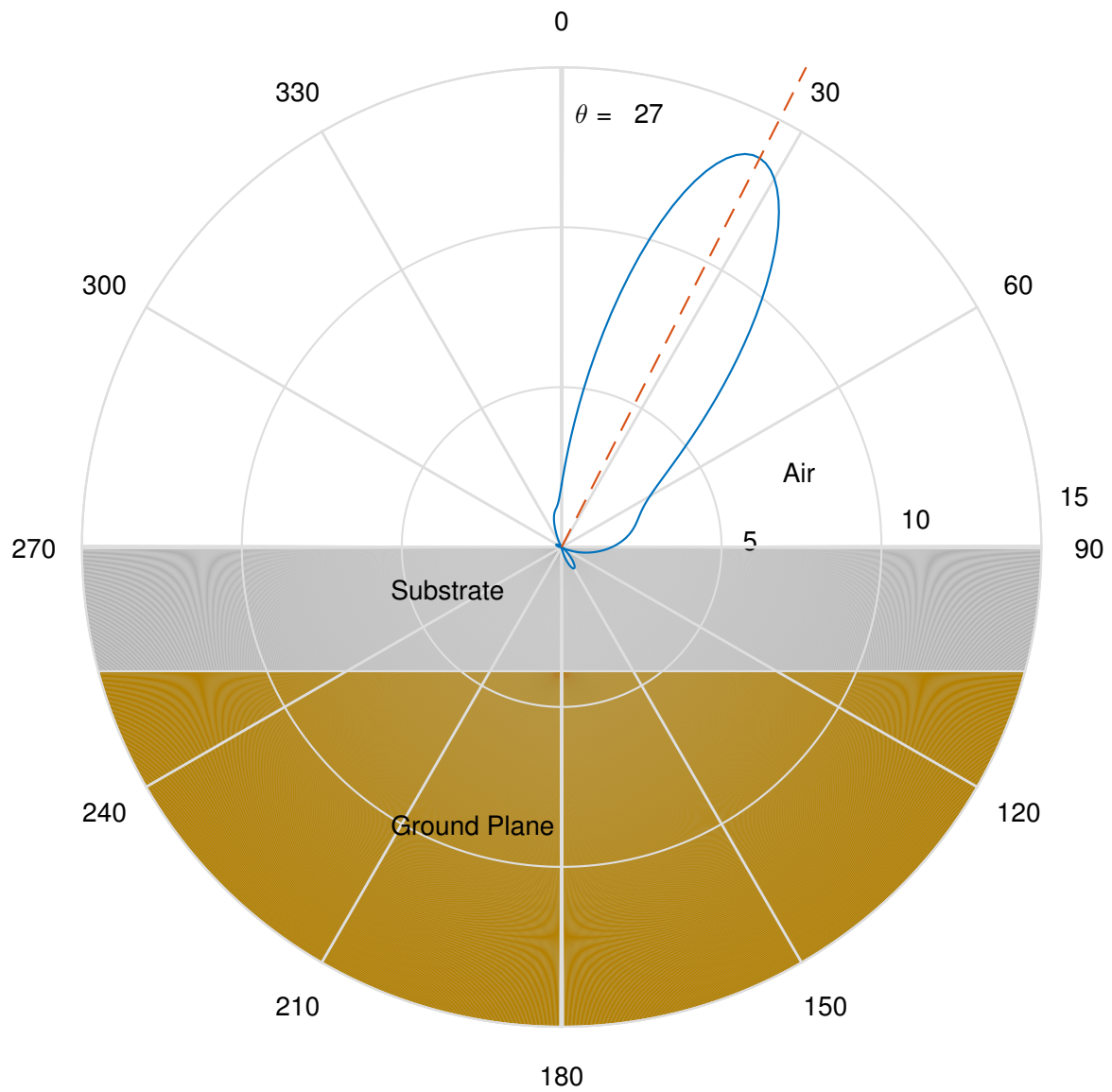


Figure 4.6: H-field directivity pattern for metal-backed plasmonic horn nanoantenna with impedance matching section.

## Chapter 5

# FABRICATIONS, OPTICAL SETUP, AND MEASUREMENTS

In this chapter we discuss fabrication process of plasmonic horn nanoantenna using E-beam lithography (EBL), our in-house developed optical setup for characterization, and characterization of these optical horn nanoantenna.

### *5.0.1 Change of geometrical parameters of the horn nanoantenna*

In order to minimize the losses in TWTL, and to integrate plasmonic horn nanoantenna with other devices developed by our lab, we modified geometrical parameters of plasmonic horn nanoantenna. For integration and minimization of losses in TWTL, we increased the gap size  $g$  from 30 nm to 220 nm, and 300 nm. In addition, we used gold (Au) as metal, and to have uniform mode inside the gap, we coated our sample with SU-8 resist. In chapter 3 and 4 we demonstrated that, by changing the material that surrounds nanoantenna, nanoantenna radiation operation and reflection coefficient changes. Thus to accommodate for these changes, we simulated nanoantenna with quartz substrate and SU-8 cladding, The new length of flares  $l$  is 850 nm,  $\theta$  is  $31^\circ$ ,  $t$  remains same as 300 nm,  $b$  is equal to 150 nm,  $c$  is equal to 115 nm, and  $a$  remains same as 1000 nm. All these geometrical changes were made in order to have: (1) gradual impedance matching between TWTL, substrate, and cladding, and (2) minimum reflection coefficient at  $1.55 \mu\text{m}$  wavelength.

### **5.1 Fabrication**

For fabrication of plasmonic horn nanoantenna, we use electronic beam lithography technique because of: required nanometer scale resolution for fabrication, direct write

without use of mask, and at hand in-house experience. For e-beam lithography, EBPG 5000+ (100keV) EBL system was used. Step by step fabrication process is given below and summary of whole process is given in Figure 5.3.

### 5.1.1 Dicing

First step of fabrication process is dicing. Quartz wafer was used as substrate with thickness of 500  $\mu\text{m}$ . Dicing was carried out with DISCO DAD 320 dicing system and quartz was diced in to 2 cm x 2 cm samples.

### 5.1.2 Cleaning

For nano-fabrication, it is very necessary to clean samples before spin coating as the sample might be contaminated due to dicing, and any organic or inorganic residue might be sitting on sample. For cleaning we used piranha solution. Piranha is the mixture of  $\text{H}_2\text{SO}_4$  and  $\text{H}_2\text{O}_2$  with ratio of 2.5-3:1 by volume. Once  $\text{H}_2\text{O}_2$  was mixed with  $\text{H}_2\text{SO}_4$ , the solution was left for 2 minutes to cool down. After cooling, quartz samples were placed in piranha solution for 5 minutes. Afterwards, samples were rinsed with DI water for 30 seconds, thrice. At the end, samples were dried with  $\text{N}_2$ .

### 5.1.3 Spin coating with PMMA

PMMA, a positive photoresist, was coated over the sample using spin coating technique. Our nanostructures' thickness  $c$  is 115 nm, therefore it is necessary to coat the sample with 250 nm to 300 nm photoresist. As a rule of thumb, ratio of photoresist thickness vs. nanostructure's, or horn nanoantenna in this case, should be 3:1, in order to achieve desired thickness of structures. For this purpose, we did bilayer resist coating. First the sample was coated with 495K A4 PMMA at the spinning rate of 5000 rpm. As a second layer, we coated 950K A2 PMMA, on the top of first layer, at the speed of 5000 rpm. It should be noted that, spinning rate is crucial parameter for determining the thickness of the photoresist. After coating, sample was backed at 170°C for 5 minutes.

#### 5.1.4 Aluminum metalization

In e-beam lithography technique, electron beam is used as source to cause chemical reaction in exposed regions of PMMA. However, quartz is insulating material and electrons accumulate on quartz surface, rather than leaving, which causes the electron beam to deflect, and causes loss of resolution. In order to overcome this limitation, we coated 15 nm thick aluminum over the PMMA coated sample with thermal evaporation process.

#### 5.1.5 E-beam lithography

As stated earlier, for direct patterning of our designs, we used Vistec EBPG 5000+ (100keV) EBL system. This system accepts .gds file, among many other extensions, of the structures which are required to be patterned. This file (.gds) was generated with Layout, CAD software, where we drew our structures to fabricate. One of the crucial step in e-beam lithography is the dose of the beam. The intensity of illuminating beam is referred as dose. In order to make soluble the area upon which e-beam is illuminated, the intensity should be optimal. If the dose is lower than optimal dose, at which solubility of PMMA molecule in developer occurs, then pattern will not be transferred properly on sample after development step. On other hand, if dose is greater than the optimal dose, chemical reaction in molecules might occur in unwanted regions of PMMA. Therefore, in order to determine the correct dose, we fabricate same devices or nanoantennas in 3x3 array on same sample, with increment of dosage between each array element, from 600  $\mu\text{C}/\text{cm}^2$  to 1000  $\mu\text{C}/\text{cm}^2$ .

#### 5.1.6 Aluminum removal

Aluminum was stripped off the e-beamed sample by putting it in TMAH based (AZ 726) developer for 1 minute. Afterwards, sample was rinsed with DI water and dried with nitrogen gas.

### 5.1.7 PMMA development

Next step is to develop the sample, after e-beam lithography. For PMMA, solution of MIBK and IPA was used as developer. Sample was placed in 1:3 (MIBK:IPA) solution for 1 minute. Afterwards, to ensure that no PMMA residue resides on sample, it was placed in 1:1 (MIBK:IPA) solution for 5 seconds. Further, sample was placed in to IPA for 30 seconds, for further cleaning.

### 5.1.8 Titanium and gold coating

Titanium and gold coating was done using thermal evaporation process using Nanovak nvt5 400 machine. Titanium is first deposited as adhesion layer between substrate and gold. At the base pressure of  $2 \times 10^{-6}$  torr, 4 nm thick titanium was coated over sample with rate of 0.2 Å/sec. Afterwards, 115 nm thickness of gold was deposited at the rate of 0.5 Å/sec.

### 5.1.9 Lift-off

To strip off the unnecessary titanium and gold from sample, and to have finalized structures, Lift-off was carried out. First of all, sample was placed on hot acetone (at 50°C) for 15 minutes. Afterwards, it was flushed and rinsed with acetone for 3 minutes. After acetone flush, sample was placed in acetone which was in-turn placed in ultrasonic cleaner for 10 minutes. Then sample was taken out from acetone, and was placed in IPA which was also available in same ultrasonic cleaner for 10 minutes. At the end sample was dried with Nitrogen gas gun.

At the end, to inspect the quality of fabrication, sample was investigated by Scanning Electron Microscopy (SEM). Figure 5.1 and 5.2 shows the images of plasmonic horn nanoantenna coupled to bend waveguide and mode converter, obtained using SEM. We found  $900 \mu\text{C}/\text{cm}^2$  as optimal dosage for plasmonic horn nanoantenna.

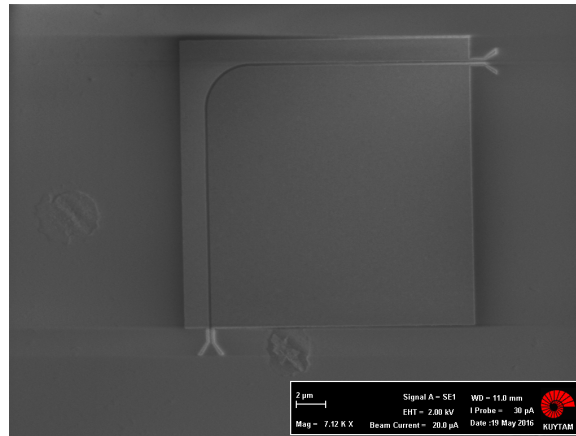


Figure 5.1: SEM image of plasmonic horn nanoantenna integrated with bend waveguide.

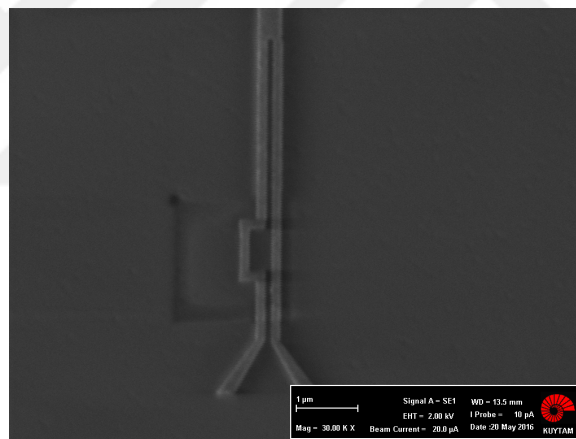


Figure 5.2: SEM image of plasmonic horn nanoantenna integrated with mode converter.

#### 5.1.10 SU-8 coating

Purpose of SU-8 coating is to have uniform mode profile in waveguides, and to reduce loss. In addition, we will use SU-8 as spacer with different thickness  $d$ , for our horn nanoantenna, between nanoantenna and ground plane. Since SU-8 is a photoresist, therefore, its thickness depends on molecular structure, density, and spin rate while

coating. Our desired thickness for SU-8 for initial characterization was 500 nm. For this purpose we used SU-8 2000 thinner to change the density of SU-8 2010 (58%) to SU-8 2000.5 (14.3%) level. Afterwards, exposure and hard bake were carried out for cross-link among the molecules.

Summary of the whole process is given is given in Figure 5.3



Figure 5.3: Fabrication process of plasmonic horn nanoantenna, in summary.

## 5.2 Optical setup

For optical characterization of plasmonic devices, we designed a home made optical setup based on reflective microscopy. Schematic for our optical setup is given in Figure 5.4. Plasmonic horn nanoantenna was characterized by its coupling efficiency to integrated bend waveguide, and transmission spectra. In detail characterization method is stated in “Measurement” section. We use Fianium broadband supercontinuum laser as our laser source. Laser is connected to acoustic optic tunable filter (AOTF), which provides two outputs labeled as NIR1 and NIR2 in Figure. Both Laser and AOTF are connected to and controlled by computer. NIR1 provides wavelength from 600 nm to 1100 nm, while NIR2 provides 1100 nm to 1800 nm of electromagnetic spectrum. Since we designed our plasmonic nanoantenna for operation around 1.55  $\mu\text{m}$  wavelength, therefore we use NIR2. We defined and designed to optical path, for NIR1 and NIR2 each, and used flip flop mirrors to switch in between those paths. In front of fiber output, we placed half-wave plate (HWP), and a polarizer (P1) after the two mirrors (M1 and M2), in order to control the polarization of the laser beam. Afterward P1, the beam passes through first iris (I1) which along with 2<sup>nd</sup> iris (I2), as shown in the Figure, are used to align the beam path between these two points. After I1, beam passes through beam splitters, labeled as B1 and B2, where B1 divides the beam into (50:50) power and only 50% of power passes through BS2. BS2 is installed to direct the light from illumination source, an infrared LED, to illuminate the sample for imaging. At this point, Laser beam and LED source both shines on sample by focusing them with objective lens (Leica) with magnification of 100x and high numerical aperture (NA) of 0.9. After reflection from sample, beam and the illuminated light are collected with same objective lens and directed through the BS2 and then BS1. Sample is placed on XYZ piezo stage, which is controlled by “THORLABS” piezo controller. Reflected beam and illumination, from BS1, is passed through second polarizer (P2), which is installed to control the polarization of reflected beam. Reflected beam is then passed through two mirrors (M3 and M4), aligned 45° to each other, in order to control the position of the reflected image on camera and detector.

Another lens is installed after after M4, which is used to transform the reflected image on a plane where we can block it with an Iris (I3), as shown in the figure. At this point a mirror (M5) is also installed either to direct the image to the camera or the detector. We use IR camera to image the sample, and for quantitative measurement we use IR photodetector which is in-turn connected to Lock-in amplifier. Detailed measurement methodology is given in “Measurements” section.

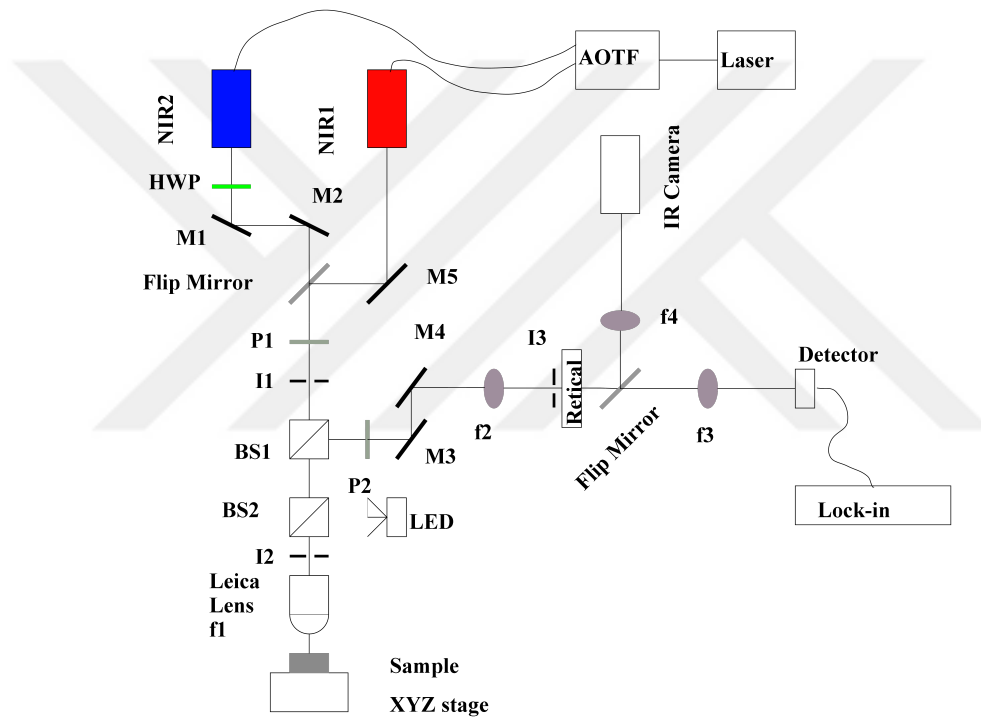


Figure 5.4: Schematics of optical setup based on reflective microscopy.

Figure 5.5 shows image of plasmonic horn nanonatenna coupled to bend waveguide captured with IR camera and our optical setup. While Figure 5.6 shows image of laser beam hitting on the sample when P1 and P2 are parallel to each other, and polarization of the beam is set horizontal (linear) polarization, and Figure 5.7 shows image of beam when P1 and P2 are in cross polarization.

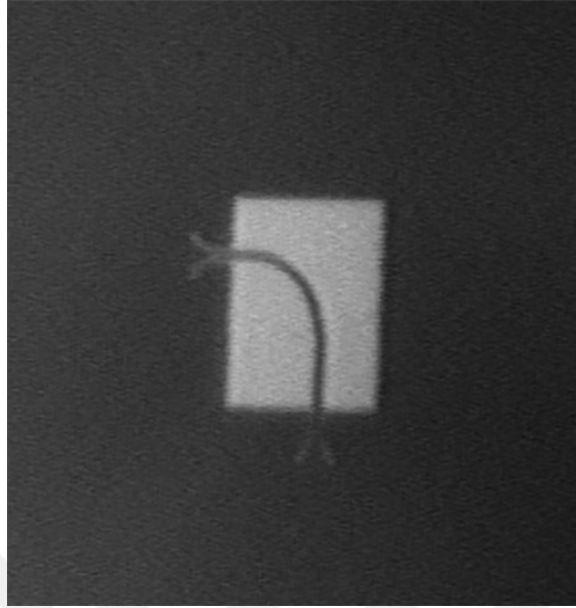


Figure 5.5: Image of plasmonic horn nanoantenna coupled to bend waveguide, taken with our optical setup.

### 5.3 Measurements

#### 5.3.1 Measurement methodology

For the measurement of plasmonic horn nanoantenna we employed method of measurement as reported in [Kriesch et al., 2013]. In this method, plasmonic horn nanoantenna were coupled to bend slot waveguides of same gap as nanoantenna i.e.  $g$  equal to 220 nm. The main purpose of using bend slot waveguide was to spatially separate input nanoantenna and output nanoantenna, and in addition to have  $90^\circ$  of difference between the polarization of these two nanoantennas. The input beam was shined at lower nanoantenna as shown in Figure 5.8 with horizontal polarization (matching with polarization of antenna). Polarization was made horizontal with P1 polarizer, as shown in Figure 5.4. After shining the beam at input nanoantenna, we observed output from output nanoantenna, on the top left side as shown in Figure 5.8. Since the output antenna has polarization in vertical i.e.  $90^\circ$  from input nanoantenna, we

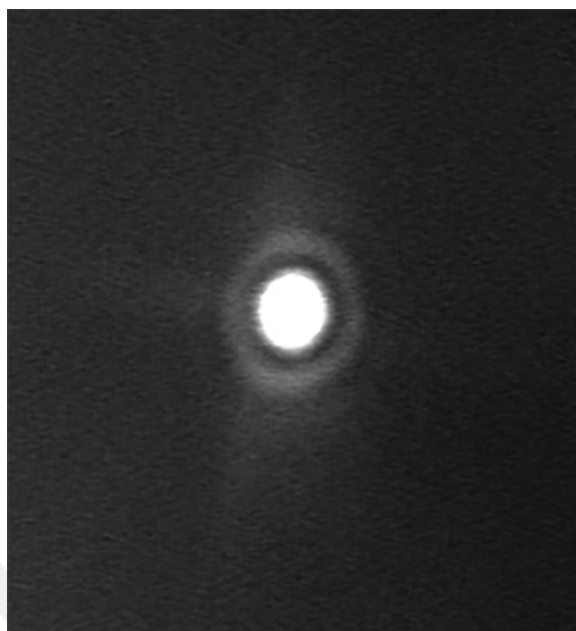


Figure 5.6: Image of beam incident on sample when P1 and P2 are in parallel.

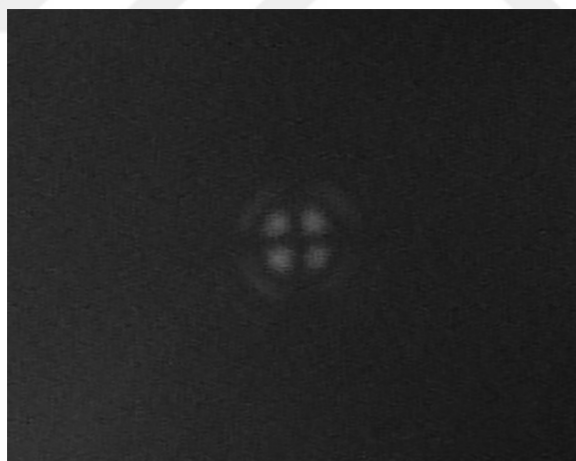


Figure 5.7: Image of beam incident on sample when P1 and P2 are in cross.

set P2 to vertical polarization, to observe output. In order to direct the output power to detector, and to make sure that only power from output nanoantenna is measured, we closed the reticle such that power from only output nanoantenna is measured.

Figure 5.8 shows image of the laser beam shining on input nanoantenna, and output from the output nanoantenna, while Figure 5.9 shows image when illumination LED was turned off (for better imaging purpose).

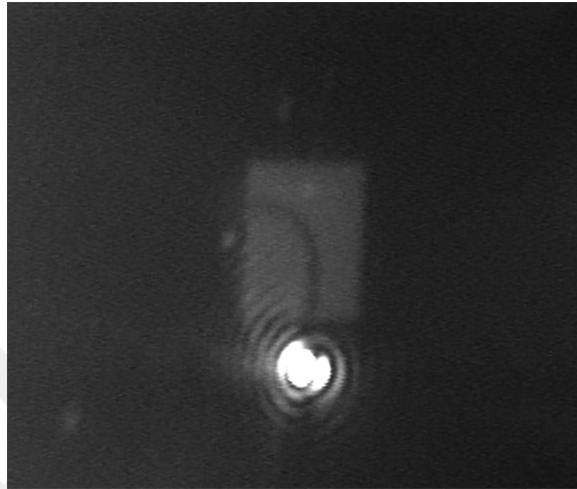


Figure 5.8: Image of plasmonic nanoantenna coupled with bend slot waveguide, with beam shining on input nanoantenna

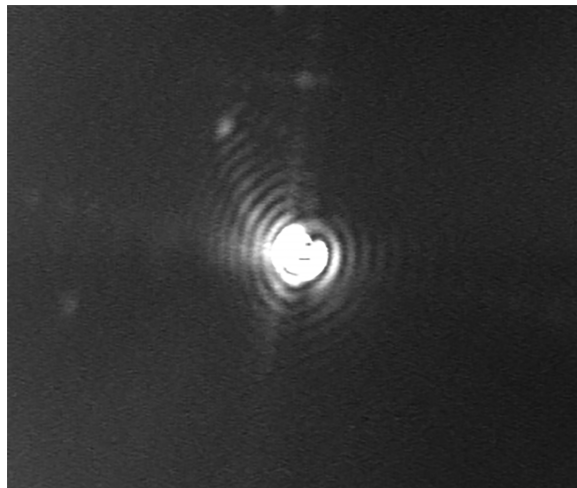


Figure 5.9: Image of plasmonic nanoantenna coupled with bend slot waveguide, with beam shining on input nanoantenna, and without illumination.

Once we have ensured that only light from output nanoantenna goes in to detector, then we swept along range of wavelength from 1200 nm to 1700 nm in order to measure the spatial transmission of whole system. Total system transmission  $T_{total}$  can be modeled as follow [Kriesch et al., 2013]

$$T_{total}(\lambda) = T_{ant1}(\lambda)T_{wg}(\lambda)T_{ant2}(\lambda) = T_{ant}(\lambda)^2T_{wg}(\lambda). \quad (5.1)$$

Here,  $\lambda$  is the wavelength,  $T_{ant1}(\lambda)$  is transmission of input antenna,  $T_{ant2}(\lambda)$  is transmission of output antenna, and  $T_{wg}(\lambda)$  is transmission of bend waveguide. Since input nanoantenna and output nanoantenna both are same, therefore, transmission of both can be given as  $T_{ant}(\lambda)^2$ . In order to take out the effect of bend waveguide, we measure couple of nanoantenna with bend waveguide systems with lengths of waveguide ranging from 8  $\mu\text{m}$  to 30  $\mu\text{m}$ , and fit an exponential function to it, in order to obtain its propagation loss and hence propagation length  $L_0$ . Then one can find transmission of waveguide with specific length as  $T(\lambda, L) = 1e^{-L/L_0}$ , where L is length of waveguide.

### 5.3.2 Measurements

In this section we present measurements carried out for characterization of horn nanoantenna. Figure 5.10 shows measured propagation length  $L_0$  of plasmonic waveguide with gap  $g$  equal to 220 nm, as a function of wavelength. At 1.55  $\mu\text{m}$  propagation length is 10.56  $\mu\text{m}$ . Total transmission  $T_{total}(\lambda)$ , for couple of plasmonic horn nanoantenna integrated with slot bend waveguide (named as A1 to A6 in legend of Figure) are given in Figure 5.11. All the devices (from A1 to A6) have same geometrical parameters, and were measured to observe the quality of fabrication and consistency of our measurement technique from device to device within same optimal dose.

Finally we calculated transmission of horn nanoantenna  $T_{ant}$  from equation 5.1. Figure 5.12 shows  $T_{ant}$  of plasmonic horn nanoantenna for the six devices (A1 to A6). It can be seen from Figure 5.12 that all the devices have almost same transmission behavior, thus the quality of fabrication is good with very less error or defect from device to device and measurement technique is also consistent. Moreover, transmission  $T_{ant}$

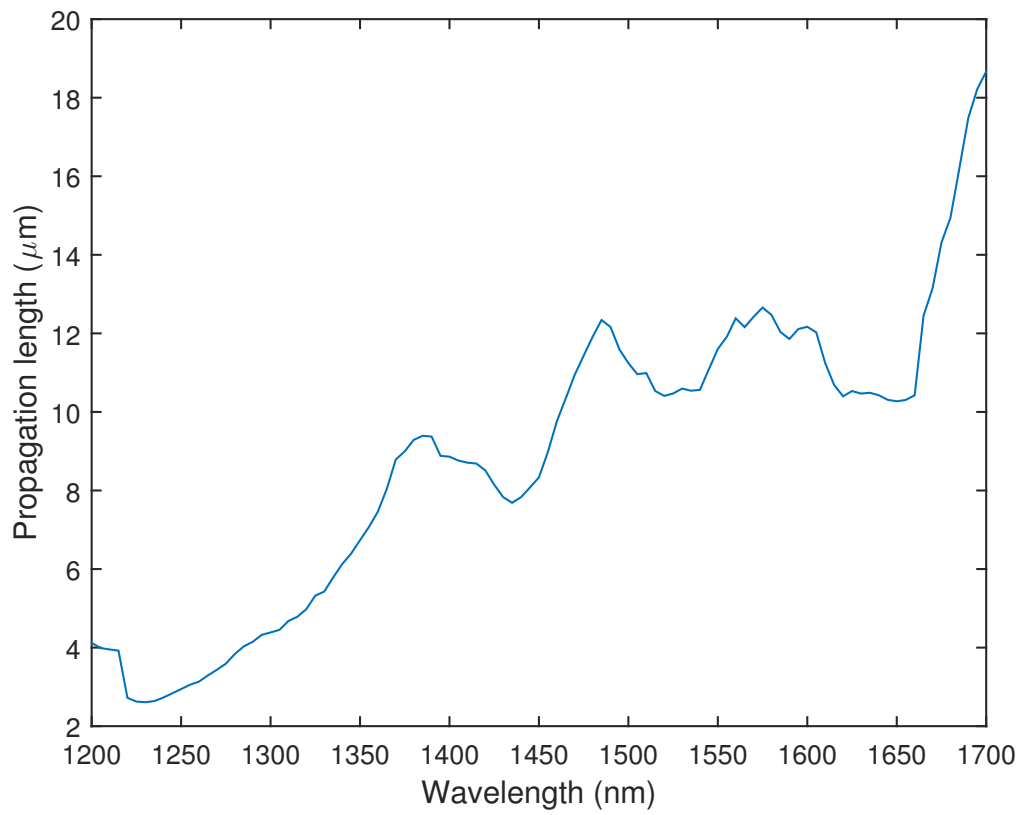


Figure 5.10: Propagation length ( $L_0$ ) of slot waveguide with  $g = 220$  nm.

is below 11% (10.78% is maximum for A5 at 1225 nm) for all the wavelength range which means that more than 89% of power is radiated into the glass substrate.

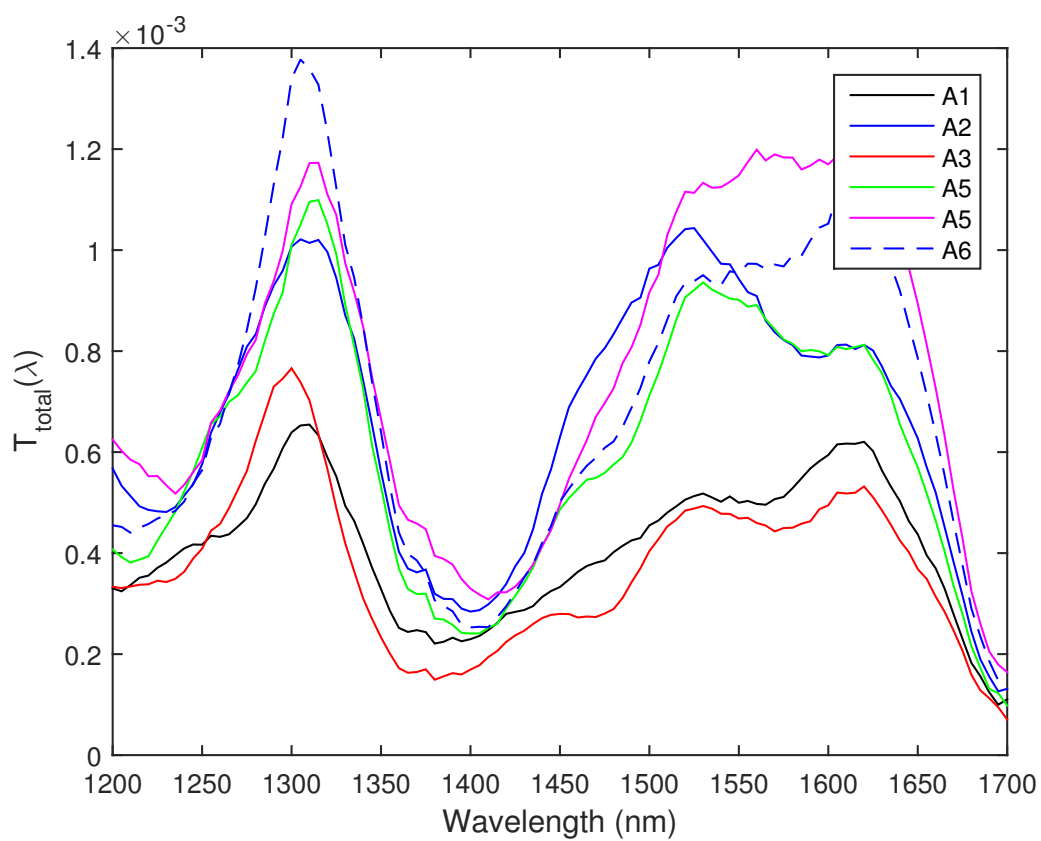


Figure 5.11:  $T_{total}(\lambda)$  of six devices with same geometrical parameters with in same optimal dose.

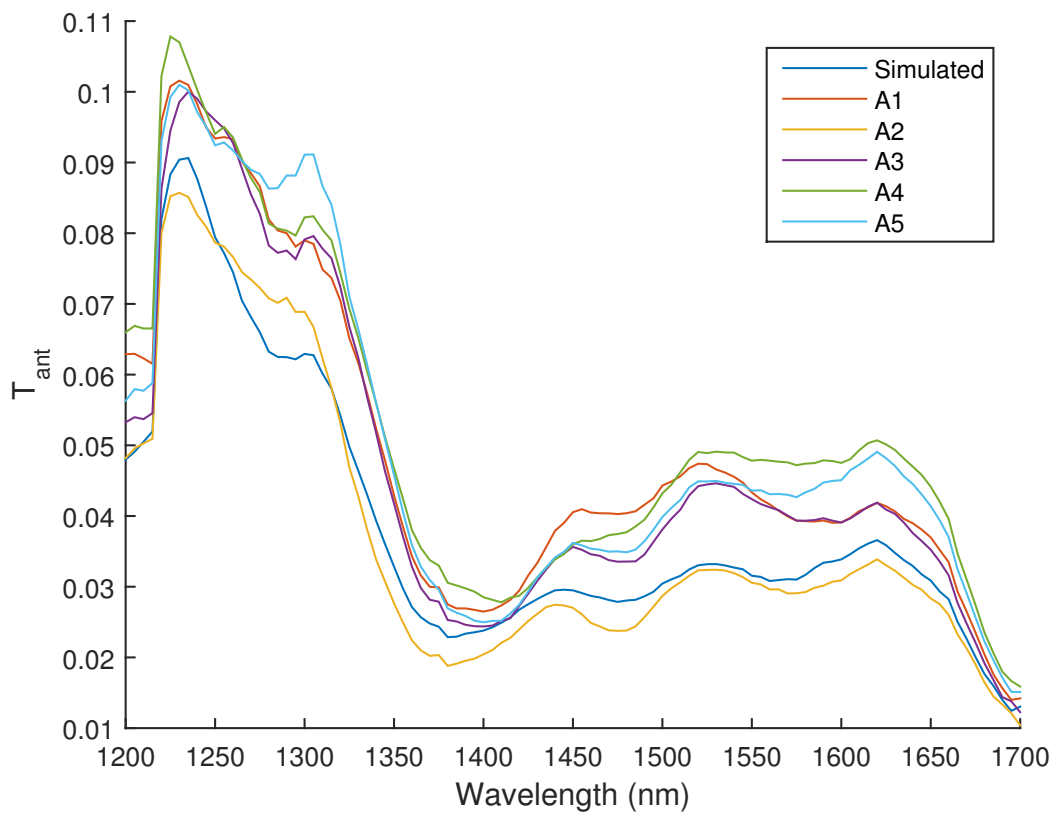


Figure 5.12: Comparison of transmission  $T_{ant}$  of plasmonic horn nanoantenna for measured results (A1 to 6).

## Chapter 6

### CONCLUSION

In this thesis, we investigated plasmonic horn nanoantenna and gave in-depth analysis of the nanoantenna in the presence of different materials surrounding it. We started our investigation by simulating plasmonic horn nanoantenna inside homogeneous medium. We demonstrated that, plasmonic horn nanoantenna efficiently transforms transmission line (TWTL) guided waves into free space propagating waves, and provides gradual impedance matching between the TWTL and free space. Plasmonic horn nanoantenna showed a broadband, highly end-fire directive radiation response with directivity of around 14.

Afterwards, we analyzed the horn nanoantenna in realistic scenario, where it was placed on the interface of two different media, glass ( $n=1.44$ ) and air ( $n=1$ ). We observed that, in this case, the nanoantenna radiated most of its radiation into glass, which has high refractive index. Horn nanoantenna no more radiated in end-fire direction, thus making it infeasible for the applications such as wireless nano-link. In addition, we demonstrated inherited impedance matched coupling between TWTL and flares of horn nanoantenna by giving result in-terms of reflection coefficient, and found it equal to 0.09 at  $1.55 \mu\text{m}$  wavelength, which means that 99 % of power is transmitted to flares. In order to control the radiation pattern of the nanoantenna, we employed metallic ground plane at the back of the glass substrate. The ground plane acted as image antenna, thus making the whole antenna system as array, where were able to achieve beam steering in broad range of radiation angles, ranging from broadside to end-fire, by changing the thickness of metal-backed substrate. However, we observed that back reflection into TWTL from flared increased due to metallic ground plane. Reflection coefficient of horn nanoantenna was found to be 0.1287 in

this case.

In order to minimize the reflection coefficient, and increase matching between TWTL and flare, we employed an impedance matching technique, which improved impedance matching by more than 70% as compared to previous value of 0.1287. With impedance matching technique, reflection coefficient was found to be 0.038 at  $1.55 \mu\text{m}$  meaning that more than 99.75% of power is transmitted to the nanoantenna. Further, in order to predict optimal parameters for impedance matching technique, we propose an analytical model. We found analytical model accurate by comparing it with simulated results, thus the model can be used to predict optimal parameters beforehand, rather than simulating whole structure which is time and memory consuming. Finally, we fabricated the nanoantenna on glass substrate with SU-8 cladding, and optically characterized it. For fabrication, we gave step-by-step detailed process. We defined our measurement methodology, and gave insight of our optical setup. We showed measured results for horn nanoantenna, where we found that horn nanoantenna has less than 11% of transmittivity in air, thus significant amount of power is radiated into the glass substrate.

### ***Funding***

This work is supported by The Scientific and Technological Research Council of Turkey - TUBITAK (Project No. 112E247), TUBITAK - BİDEB 2215 - Graduate Scholarship Program for International Students, and Koç University.

## BIBLIOGRAPHY

- [Ahmed and Gordon, 2011] Ahmed, A. and Gordon, R. (2011). Directivity enhanced raman spectroscopy using nanoantennas. *Nano Letters*, 11(4):1800–1803. PMID: 21428381.
- [Alù and Engheta, 2010] Alù, A. and Engheta, N. (2010). Wireless at the nanoscale: Optical interconnects using matched nanoantennas. *Phys. Rev. Lett.*, 104:213902.
- [Anker et al., 2008] Anker, J. N., Hall, W. P., Lyandres, O., Shah, N. C., Zhao, J., and Van Duyne, R. P. (2008). Biosensing with plasmonic nanosensors. *Nat Mater*, 7(6):442–453.
- [Atwater, 2007] Atwater, H. A. (2007). The promise of plasmonics. *Scientific American*, 296(4):56–62.
- [Atwater and Polman, 2010] Atwater, H. A. and Polman, A. (2010). Plasmonics for improved photovoltaic devices. *Nat Mater*, 9(3):205–213.
- [Balanis, 2016] Balanis, C. A. (2016). *Antenna theory: analysis and design*. John Wiley & Sons.
- [Bharadwaj et al., 2011] Bharadwaj, P., Beams, R., and Novotny, L. (2011). Nanoscale spectroscopy with optical antennas. *Chem. Sci.*, 2:136–140.
- [Bohren and Huffman, 2008] Bohren, C. F. and Huffman, D. R. (2008). *Absorption and scattering of light by small particles*. John Wiley & Sons.
- [Born and Wolf, 2000] Born, M. and Wolf, E. (2000). *Principles of optics: electromagnetic theory of propagation, interference and diffraction of light*. CUP Archive.

- [Burke et al., 1986] Burke, J., Stegeman, G., and Tamir, T. (1986). Surface-polariton-like waves guided by thin, lossy metal films. *Physical Review B*, 33(8):5186.
- [Curto et al., 2010] Curto, A. G., Volpe, G., Taminiau, T. H., Kreuzer, M. P., Quidant, R., and van Hulst, N. F. (2010). Unidirectional emission of a quantum dot coupled to a nanoantenna. *Science*, 329(5994):930–933.
- [Dionne et al., 2006] Dionne, J., Sweatlock, L., Atwater, H., and Polman, A. (2006). Plasmon slot waveguides: Towards chip-scale propagation with subwavelength-scale localization. *Physical Review B*, 73(3):035407.
- [Dionne and Atwater, 2012] Dionne, J. A. and Atwater, H. A. (2012). Plasmonics: metal-worthy methods and materials in nanophotonics. *MRS Bulletin*, 37(08):717–724.
- [Economou, 1969] Economou, E. (1969). Surface plasmons in thin films. *Physical review*, 182(2):539.
- [G. et al., 2011] G., L., W., C., EghlidiH., KukuraP., LettowR., RennA., SandoghdarV., and GotzingerS. (2011). A planar dielectric antenna for directional single-photon emission and near-unity collection efficiency. *Nat Photon*, 5(3):166–169.
- [Ghadarghadr et al., 2009] Ghadarghadr, S., Hao, Z., and Mosallaei, H. (2009). Plasmonic array nanoantennas on layered substrates: modeling and radiation characteristics. *Opt. Express*, 17(21):18556–18570.
- [Ginzburg and Orenstein, 2007] Ginzburg, P. and Orenstein, M. (2007). Plasmonic transmission lines: from micro to nano scale with  $\lambda/4$  impedance matching. *Opt. Express*, 15(11):6762–6767.
- [Gramotnev and Bozhevolnyi, 2010] Gramotnev, D. K. and Bozhevolnyi, S. I. (2010). Plasmonics beyond the diffraction limit. *Nature photonics*, 4(2):83–91.

- [Hosseini et al., 2008] Hosseini, A., Nejati, H., and Massoud, Y. (2008). An analytical model for characteristic impedance in nanostrip plasmonic waveguides. In *2008 IEEE International Symposium on Circuits and Systems*, pages 2346–2349.
- [Huang et al., 2009] Huang, J.-S., Feichtner, T., Biagioni, P., and Hecht, B. (2009). Impedance matching and emission properties of nanoantennas in an optical nanocircuit. *Nano letters*, 9(5):1897–1902.
- [Johnson and Christy, 1972a] Johnson, P. B. and Christy, R.-W. (1972a). Optical constants of the noble metals. *Physical review B*, 6(12):4370.
- [Johnson and Christy, 1972b] Johnson, P. B. and Christy, R. W. (1972b). Optical constants of the noble metals. *Phys. Rev. B*, 6:4370–4379.
- [Kauranen and Zayats, 2012] Kauranen, M. and Zayats, A. V. (2012). Nonlinear plasmonics. *Nat Photon*, 6(11):737–748.
- [Knight et al., 2011] Knight, M. W., Sobhani, H., Nordlander, P., and Halas, N. J. (2011). Photodetection with active optical antennas. *Science*, 332(6030):702–704.
- [Kriesch et al., 2013] Kriesch, A., Burgos, S. P., Ploss, D., Pfeifer, H., Atwater, H. A., and Peschel, U. (2013). Functional plasmonic nanocircuits with low insertion and propagation losses. *Nano letters*, 13(9):4539–4545.
- [Ly-Gagnon et al., 2008] Ly-Gagnon, D. S., Kocabas, S. E., and Miller, D. A. B. (2008). Characteristic impedance model for plasmonic metal slot waveguides. *IEEE Journal of Selected Topics in Quantum Electronics*, 14(6):1473–1478.
- [Min et al., 2011] Min, Q., Pang, Y., Collins, D. J., Kuklev, N. A., Gottselig, K., Steuerman, D. W., and Gordon, R. (2011). Substrate-based platform for boosting the surface-enhanced raman of plasmonic nanoparticles. *Opt. Express*, 19(2):1648–1655.

- [Novotny, 2007] Novotny, L. (2007). Effective wavelength scaling for optical antennas. *Phys. Rev. Lett.*, 98:266802.
- [Palik, 1998] Palik, E. D. (1998). *Handbook of optical constants of solids*, volume 3. Academic press.
- [Raether, 1988] Raether, H. (1988). *Surface plasmons on smooth surfaces*. Springer.
- [Ramaccia et al., 2011] Ramaccia, D., Bilotti, F., Toscano, A., and Massaro, A. (2011). Efficient and wideband horn nanoantenna. *Opt. Lett.*, 36(10):1743–1745.
- [Sachkou et al., 2011] Sachkou, Y., Andryieuski, A., and Lavrinenko, A. V. (2011). Impedance conjugate matching of plasmonic nanoantenna in optical nanocircuits. In *ELMAR, 2011 Proceedings*, pages 389–391.
- [Seok et al., 2011] Seok, T. J., Jamshidi, A., Kim, M., Dhuey, S., Lakhani, A., Choo, H., Schuck, P. J., Cabrini, S., Schwartzberg, A. M., Bokor, J., Yablonovitch, E., and Wu, M. C. (2011). Radiation engineering of optical antennas for maximum field enhancement. *Nano Letters*, 11(7):2606–2610. PMID: 21648393.
- [Solís et al., 2013] Solís, D. M., Taboada, J. M., Obelleiro, F., and Landesa, L. (2013). Optimization of an optical wireless nanolink using directive nanoantennas. *Opt. Express*, 21(2):2369–2377.
- [Stratton, 2007] Stratton, J. A. (2007). *Electromagnetic theory*. John Wiley & Sons.
- [Taflove, 2000] Taflove, A. (2000). *Computational electrodynamics*.
- [Veronis and Fan, 2007] Veronis, G. and Fan, S. (2007). Modes of subwavelength plasmonic slot waveguides. *Journal of Lightwave Technology*, 25(9):2511–2521.
- [Veronis et al., 2009] Veronis, G., Kocaba, ü. E., Miller, D. A. B., and Fan, S. (2009). Modeling of plasmonic waveguide components and networks. *Journal of Computational and Theoretical Nanoscience*, 6(8):1808–1826.

- [Xi et al., 2013] Xi, Z., Lu, Y., Yao, P., Yu, W., Wang, P., and Ming, H. (2013). Controllable directive radiation of a circularly polarized dipole above planar metal surface. *Opt. Express*, 21(25):30327–30335.
- [Xu et al., 2011] Xu, Y., Miroschnichenko, A. E., Lan, S., Guo, Q., and Wu, L.-J. (2011). Impedance matching induce high transmission and flat response band-pass plasmonic waveguides. *Plasmonics*, 6(2):337–343.
- [Yang et al., 2016] Yang, Y., Li, Q., and Qiu, M. (2016). Broadband nanophotonic wireless links and networks using on-chip integrated plasmonic antennas. 6.
- [Yang et al., 2014] Yang, Y., Zhao, D., Gong, H., Li, Q., and Qiu, M. (2014). Plasmonic sectoral horn nanoantennas. *Opt. Lett.*, 39(11):3204–3207.